

Improved Methods for Rapid and Scalable Tissue Clearing and Labeling

by

Evan Murray

B.S. Biology

Massachusetts Institute of Technology, 2013

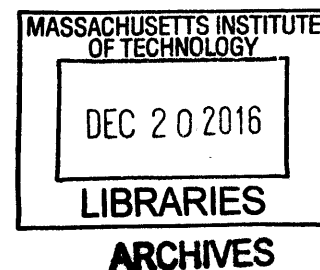
Submitted to the department of Brain and Cognitive Sciences  
in partial fulfillment of the requirements for the degree of

Master of Science in Neuroscience

at the

MASSACHUSETTS INSTITUTE OF TECHNOLOGY

September 2016



© 2016 Massachusetts Institute of Technology. All rights reserved.

Signature redacted

Signature of Author: \_\_\_\_\_

Department of Brain and Cognitive Sciences

August 12, 2016

Signature redacted

Certified by: \_\_\_\_\_

Kwanghun Chung

Samuel A. Goldblith Career Development Assistant Professor of Chemical Engineering

Thesis Supervisor

Signature redacted

Accepted by: \_\_\_\_\_

Matthew A. Wilson

Sherman Fairchild Professor of Neuroscience and Picower Scholar

Director of Graduate Education for Brain and Cognitive Sciences



77 Massachusetts Avenue  
Cambridge, MA 02139  
<http://libraries.mit.edu/ask>

## **DISCLAIMER NOTICE**

Due to the condition of the original material, there are unavoidable flaws in this reproduction. We have made every effort possible to provide you with the best copy available.

Thank you.

**The images contained in this document are of the best quality available.**

Improved Methods for Rapid and Scalable Tissue Clearing and Processing

by

Evan Murray

Submitted to the Department of Brain and Cognitive Sciences  
on August 12, 2016 in partial fulfillment of the  
requirements for the Degree of Master of Science in  
Neuroscience

ABSTRACT

Combined measurement of diverse molecular and anatomical traits that span multiple levels remains a major challenge in biology. Here, we introduce a simple method that enables proteomic imaging for scalable, integrated, high-dimensional phenotyping of both animal tissues and human clinical samples. This method, termed SWITCH, uniformly secures tissue architecture, native biomolecules, and antigenicity across an entire system by synchronizing the tissue preservation reaction. The heat- and chemical-resistant nature of the resulting framework permits multiple rounds (>20) of relabeling. We have performed 22 rounds of labeling of a single tissue with precise co-registration of multiple datasets. Furthermore, SWITCH synchronizes labeling reactions to improve probe penetration depth and uniformity of staining. With SWITCH, we performed combinatorial protein expression profiling of the human cortex and also interrogated the geometric structure of the fiber pathways in mouse brains. Such integrated high-dimensional information may accelerate our understanding of biological systems at multiple levels.

Thesis Supervisor: Kwanghun Chung  
Title: Assistant Professor of Chemical Engineering

## Acknowledgments

I would like to thank Naveed Bakh, Sung-Yon Kim, Justin Swaney, Taeyun Ku, and Meg McCue for helpful conversations, assistance for experiments, and suggestions on the work presented in this thesis. I would also like to thank Taeyun Ku and Daniel Goodwin for extraordinary computational efforts without which this would not have been possible.

Finally, I extend thanks to Professor Chung for his expert guidance throughout this work as well as his unwavering optimism.

## INTRODUCTION

Biological systems are comprised of vast numbers of molecules, cell types, and intricate tissue organizations (Alivisatos et al., 2013; Kasthuri et al., 2015; Yuste, 2015). Understanding the complex interactions of these components is essential for many fields of biology and often requires high-dimensional information across many scales. Although it is desirable to obtain such information from the same tissue due to large individual variations, combined measurement of many molecular and anatomical traits remains an unmet goal in biology despite the remarkable success of current pioneering methods, such as array tomography (Micheva et al., 2010; Rah et al., 2013).

Rapidly evolving tissue-clearing techniques may enable multiplexed labeling and imaging of intact samples using light microscopy (Chung et al., 2013; Chung and Deisseroth, 2013; Renier et al., 2014; Richardson & Lichtman, 2015; Susaki et al., 2014). For instance, the CLARITY technique has demonstrated three rounds of immunostaining of mouse brain tissue (Chung et al., 2013). However, we have noticed that the polyacrylamide-based framework loses structural integrity upon repeated exposure to the elution condition. Recent reports also suggest that preservation of antigenicity in the CLARITY method may not be optimal (Renier et al., 2014). Furthermore, the necessary tissue-gel hybridization step requires delivery of charged thermal initiators with limited diffusivity and stability. This necessity imposes a limit on the tissue size that can be processed without the use of transcatheter perfusion.

We set our goal to develop a simple, scalable, and generalizable tissue-processing method for proteomic imaging of intact biological systems. To achieve this, we created SWITCH (**S**ystem-**W**ide control of **I**nteraction **T**ime and kinetics of **C**hemicals), which tightly controls a broad range of chemical reactions in tissue processing via a set of buffers: a SWITCH-On buffer that facilitates chemical reactions between exogenous chemicals and endogenous biomolecules, and a SWITCH-Off buffer that suppresses the

reactions. SWITCH-mediated fixation transforms tissue into a heat- and chemical-resistant hybrid while preserving tissue architecture, native molecules, and their antigenicity to a degree suitable for multiplexed proteomic imaging. The hybrids can be rapidly cleared at high temperature without damage. The method does not require perfusion and is thus applicable to both animal and large human samples. In molecular labeling of the processed samples, SWITCH controls probe-target binding kinetics to improve probe penetration depth and the uniformity of molecular labeling. This method is simple, passive, and does not require any special equipment or reagents.

Using SWITCH, we demonstrated that a minimum of 22 rounds of molecular labeling of a banked postmortem human tissue with precise co-registration of multiple datasets at single-cell resolution is possible. We also demonstrated extraction of a wide range of system variables, such as various cell types and microvasculature from a single sample. In summary, we have developed simple tissue processing methods and a volumetric co-registration algorithm that can be readily adopted by most laboratories for scalable proteomic imaging of intact biological systems.

## RESULTS

### **Synchronizing Dialdehyde-tissue-gel Formation Enables Scalable Tissue Preservation.**

First, we sought to develop a way to transform animal and human samples into a mechanically and chemically stable form for multiplexed imaging. We hypothesized that small, non-ionic, multifunctional crosslinkers might satisfy two key requirements for such a transformation: (1) rapid penetration without the use of perfusion and (2) a high degree of molecular crosslinking to improve sample durability (Hopwood, 1972; Sung et al., 1996). Among many options, we chose to evaluate the following owing to their small size and high water solubility (Figure 1A): ethylene glycol diglycidyl ether (EGDGE), dipropylene glycol diglycidyl ether (GE23), 1,4-butanediol diglycidyl ether (GE21), glycerol polyglycidyl ether (EX-313), and glutaraldehyde (GA).

We found that all of these chemicals except GE23 formed a solid gel upon incubation with 15% bovine serum albumin (BSA), indicating the formation of a crosslinked network (Figure 1B). We examined the stability of the gels along with polyacrylamide (AA)-BSA gels by measuring the change in their volume after incubation in a 200 mM SDS solution heated to 80°C (elution condition). AA-BSA gels swelled and became fragile after exposure to the harsh condition (Figures 1B and 1C), whereas multi-functional fixative-BSA gels maintained their structural integrity. In particular, GA-BSA gels showed minimal volume change at a wide range of BSA and GA concentrations, whereas others only gelled at high protein concentrations (Figure 1C). This result indicates that multifunctional fixatives alone might be sufficient to form a stable matrix that can withstand the harsh elution condition. However, because the average protein content throughout mouse brain samples is around 10% and may be lower within certain regions, we decided that GA is the crosslinker most likely to form a uniform framework throughout all regions of a sample.

Next, we asked whether GA can rapidly penetrate tissue to form a uniform tissue-gel without the use of perfusion, which is required for processing most human clinical samples. We incubated a non-fixed whole adult rat brain in PBS containing 1% GA for 2 days and characterized the GA penetration depth and gel formation. Although the small size of GA should make it highly mobile, only the outer layer of the brain was fixed (Figure 1F). When a coronal slice from the middle of the brain was exposed to the elution condition, the core of the tissue completely disintegrated, indicating that no gel matrix had formed in the center of the brain (Figure 1F). Limited GA penetration has significantly hampered its use in preserving large postmortem tissues (Hopwood, 1967). We suspect that rapid reaction of GA with native biomolecules within the outer layer of the brain may cause depletion of GA molecules before they can reach the core.

To overcome this issue, we sought to control the reaction kinetics of GA and biomolecules throughout the system using the SWITCH approach to achieve uniform tissue preservation. We noted that the GA reaction rate is pH-dependent (Hopwood, 1970). Indeed, when we titrated solutions of GA and BSA to pH 3, GA-BSA gel formation time increased by nearly 200-fold (Figure 1D). Using this pH dependence, we were able to disperse GA uniformly throughout a sample by switching off the crosslinking reaction with a low-pH buffer (Figure 1E, left). After 2 days of incubation at low pH, we switched on sample-wide GA-tissue crosslinking by shifting the pH of the sample to a neutral pH (Figure 1E, right). Using this passive buffer-switching approach, we were able to achieve complete GA penetration and uniform gel formation throughout the entire rat brain (Figure 1F).

### **Dialdehyde-tissue-gel Preserves Structural and Molecular Information Effectively.**

We next asked whether the GA-tissue-gel has mechanical and chemical properties desirable for multiplexing-based proteomic imaging. Proteomic imaging requires (1) high preservation of endogenous biomolecules and their antigenicity, (2) high structural integrity, and (3) minimal tissue damage during repeated cycles of destaining, labeling, and imaging processes.

We first tested whether endogenous biomolecules are well preserved by measuring protein loss after clearing (see supplemental methods). We found that control tissues lost an average of 30–40% protein and AA-tissue-gel lost 10–20%, but GA-tissue-gel slices lost only 3–5% of their protein content (Figure 1G).

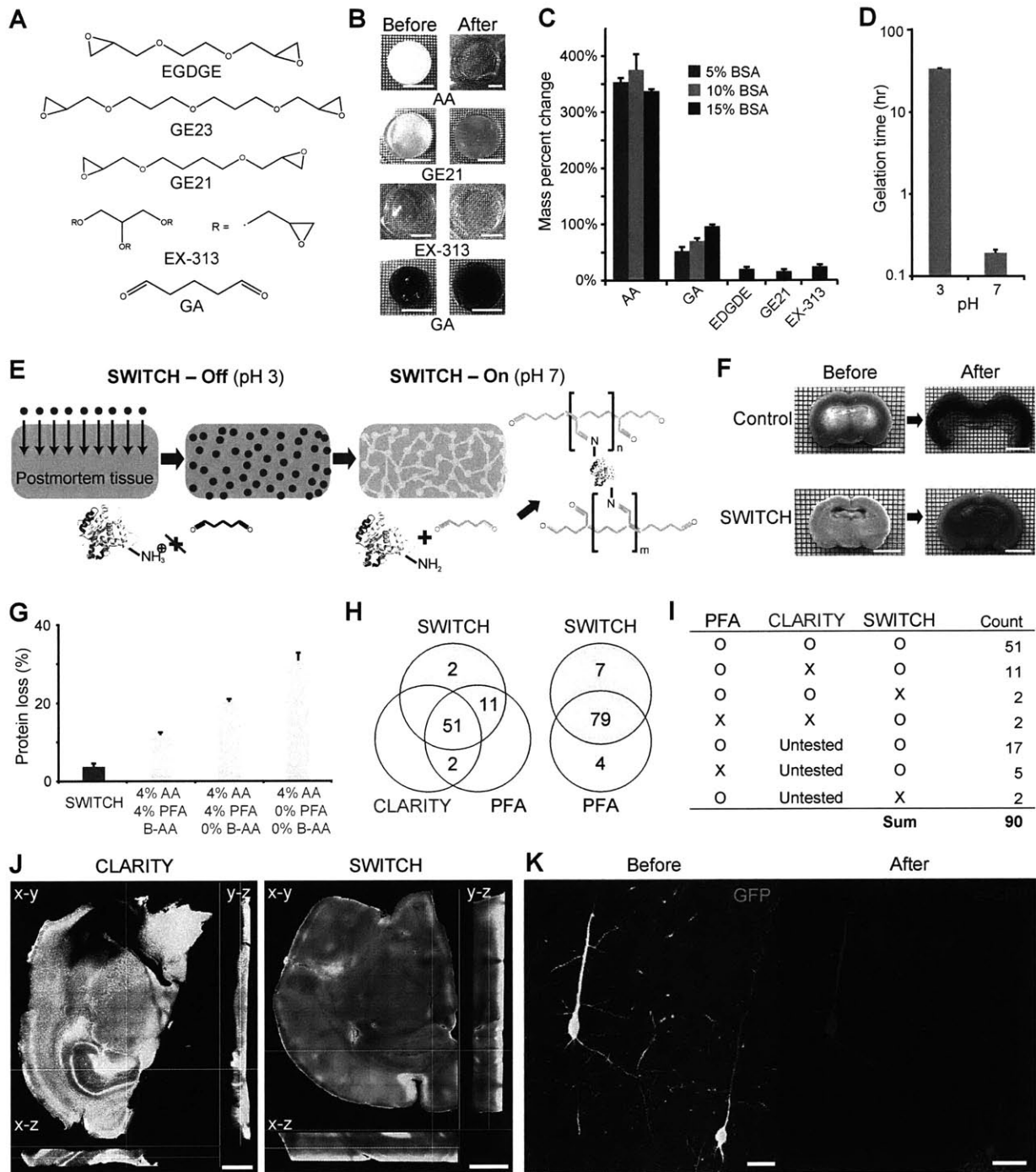
We next asked whether antigenicity of the retained biomolecules is well preserved. We tested 90 antibodies, targeting biomolecules of different sizes (single amino acid to proteins) and subcellular localizations (membrane bound, cytoplasm, nucleus, synapses). Surprisingly, 86 of 90 antibodies were compatible with GA-tissue-gel (Figures 1H and 1I). Note that even small molecules, such as dopamine, which are not typically compatible with PFA-fixation, were observable in GA-tissue-gel after the complete removal of lipid bilayers. These biomolecules were stable against heat and chemical treatment, and their antigenicity was well preserved after exposure to elution conditions.

Good structural preservation is essential for resolving protein location with high precision and for studying molecular interrelationships. To characterize the macroscale structural preservation of the samples, we cleared 1-mm-thick tissue blocks using the elution condition and visualized their structural deformation (Figure 1J). The PFA-only tissue completely disintegrated. Even the AA-tissue-gel exhibited large deformations overall. GA-tissue-gel, however, showed no signs of structural damage throughout the entirety of the sample.

We next examined structural preservation on a microscopic scale. We imaged green fluorescent protein (GFP)-expressing neurons in the cortex of a PFA-fixed 1-mm-thick thy1-EGFP M line block (Figure 1K). We then SWITCH-processed the tissue, cleared it using the harsh elution condition, stained it against GFP, and imaged the same neurons. As shown in Figure 1K, the microscopic morphology of the neurons was well preserved throughout the entire process. These results show GA-tissue-gel may be ideal for highly multiplexed structural and molecular phenotyping.

**Figure 1. Synchronizing Dialdehyde-tissue-gel Formation Enables Scalable Tissue Preservation.** (A) Chemical structures of various multifunctional fixatives. (B) Crosslinked protein gels before and after exposure to the elution condition. Scale bars, 10 mm. Polyacrylamide (AA) gel swelled and became fragile, whereas multifunctional fixative gels remained intact with minimal expansion. (C) Mass percent change of crosslinked protein gels after exposure to the harsh condition. EDGDE, GE21, and EX-313 were incapable of forming gels at low BSA concentration. Error bars show mean  $\pm$  SD. (D) The gelation time for protein gels crosslinked with GA is nearly 200-fold higher at pH 3 than it is at neutral pH at 4°C. Error bars show mean  $\pm$  SD. (E) Schematic diagram illustrating the process of scalable and uniform tissue-gel formation without perfusion using SWITCH. GA molecules diffuse into an intact tissue without reacting with biomolecules in pH 3 buffer (SWITCH-Off step). When GA is uniformly dispersed throughout the tissue, the sample is moved to pH 7 buffer (SWITCH-On step) to initiate global gelation/fixation and achieve uniform tissue preservation. (F) Coronal slices from the middle of whole rat brains passively fixed with (bottom) or without (top) SWITCH. After fixation, the middle coronal slices were cut and incubated in the elution condition for 1 hr. The core of the control slice completely disintegrated, whereas the SWITCH-processed slices remained intact. Scale bars, 6 mm. (G) Only ~3% of proteins are lost in SWITCH-processed brain tissues as opposed to ~10–30% with AA-based methods. Error bars show mean  $\pm$  SD. (H and I) Antigenicity of proteins is well preserved throughout the clearing process in SWITCH. Of the antibodies tested, 86 of 90 are compatible with SWITCH. (J and K) SWITCH-mediated fixation maximally preserves macroscopic (J) and microscopic (K) structures throughout the elution process. (J) Cross-sectional images of 1-mm-thick mouse coronal slices after exposure to the elution condition. The CLARITY-processed tissue shows significant tissue deformation and collapse, whereas the SWITCH-processed tissue is highly uniform with no signs of macroscopic deformation. Z-step size, 20  $\mu$ m; 10 $\times$ , 0.3 NA, water-immersion objective. Scale bars, 1 mm. (K) GFP-expressing neurons in the cortex of Thy-1-EGFP mouse brain before and after exposure to the elution condition and anti-GFP staining. 25 $\times$ , 0.95 NA, water-immersion objective. Scale bars, 30  $\mu$ m.

**Figure 1. Synchronizing dialdehyde-tissue-gel formation enables scalable tissue preservation**





## **SWITCH and Robust Computational Algorithms Enable Highly Multiplexed Imaging at Single-Cell Resolution.**

Interrogating the three-dimensional (3D) distribution of molecules, cells, and the overall tissue organization requires precise co-registration of multiple volume images. We first asked if simple manual overlay of two datasets allows precise co-registration. As a stringent test, we used datasets from multi-round imaging of a SWITCH-processed 100- $\mu\text{m}$ -thick human brain slice (100  $\mu\text{m}$   $\times$  3,200  $\mu\text{m}$   $\times$  3,200  $\mu\text{m}$ ) (Figure 2A). The high aspect ratio of such tissues makes it more prone to physical warping, which renders co-registration particularly challenging. We first stained the tissue using DAPI and anti-parvalbumin (PV) antibody. The slice was then enclosed in a space larger than the tissue to exaggerate possible tissue deformation in the mounting process (Figure 2B). After imaging, the sample was exposed to the elution condition overnight (O/N) to completely remove imaged probes. We then restained the tissue using the same probes and repeated the imaging process. Note that only GA-tissue-gels could maintain their integrity against the elution treatment. Both AA-tissue-gels and PFA-fixed samples deteriorated rapidly in the same condition.

As predicted, a large degree of tissue warping in the mounting process (Figure 2C) made manual overlay insufficient for the task of interrogating a tissue across multiple staining rounds. To achieve precise co-registration of volume images in the presence of such high-degree warping, we custom-designed a robust computational software based on a feature-detection approach that was ideal for our experimental procedure (Figure 2D). Each staining round contained one fluorescence channel devoted to a lectin stain because the morphology of blood vessels creates distinctive keypoints that computer vision algorithms are well suited to identify. With the keypoints, the algorithm warps the tissue in a physically plausible manner into the correct position (see supplemental methods).

As a stringent test of the algorithm, we used the same SWITCH-processed human sample with the high aspect ratio (Figure 2A). For each round, the sample was stained with DAPI, lectin, and one antibody to label a target protein. Although at least three antibodies can be used for each round in addition to lectin and DAPI, we chose to use one antibody for each round to eliminate any possible cross-talk between channels. After acquiring images, we destained the sample and began the next round of labeling. We repeated the above procedure 22 times using markers for various cell types (Figure 2H; Table 1). Staining was not successful in every round due to the use of non-validated antibodies, sub-optimal staining conditions, or human error, all of which often occur in general laboratory settings and can result in the loss of important samples. However, a SWITCH-processed sample is free from this issue as the tissue can be washed and reused repeatedly.

We were able to successfully co-register all 9 datasets with successful staining (Figures 2E and 2H). We asked whether changes in the sample might be occurring between staining rounds. To test this, we repeated staining with anti-PV antibodies in rounds 7 and 19 and co-registered the resulting datasets. Even when separated by 12 rounds of labeling, we were able to achieve single-cell accuracy of registration with 99% agreement between the two rounds (Figure 2G).

We next performed joint statistical analysis of the integrated cross-talk-free dataset to extract diverse phenotypic information from human brain (Figure 3). We included lectin, GFAP, NeuN, SMI-32, and three calcium-binding protein channels—calbindin (CB), calretinin (CR), and PV—in the quantitative analysis. First, we used semi-automated algorithms to identify blood vessels and cells expressing the target antigens (Figures 3A and 3B) and extract their spatial (x, y, z coordinates) and morphological (e.g., cell soma size) information. Density and size profiles of NeuN-positive cells (Figures 3C and 3D) enabled us to define the cortical layers (Figure 3A) according to established criteria (De Sousa et al., 2010). NeuN<sup>+</sup>

density was high in cortical layers II and IV, with characteristic small cells (NeuN in Figures 3A, 3C, 3D, and 3H). Large NeuN<sup>+</sup> neurons were concentrated in layers III and V. A portion of these were large pyramidal neurons positive for SMI-32 (Figures 3A, 3E, and 3H). CB<sup>+</sup>, CR<sup>+</sup>, and PV<sup>+</sup> cells also showed distinct distribution patterns along the cortical axis (Figures 3A and 3D), in agreement with previous studies (DeFelipe et al., 1999; Leuba et al., 1998).

We next performed unbiased combinatorial expression profiling with the 6 cell-type specific proteins (GFAP, NeuN, SMI-32, CB, CR, PV). Among 63 possible combinations, 16 were found (Table S2). We identified sub-populations of CB<sup>+</sup>/CR<sup>+</sup> and CB<sup>+</sup>/PV<sup>+</sup> cells, but no CR<sup>+</sup>/PV<sup>+</sup> or CB<sup>+</sup>/CR<sup>+</sup>/PV<sup>+</sup> cells (Figures 3F, 3H, and 3I), in agreement with a previous report regarding mouse visual cortex (Gonchar et al., 2007). Interestingly, we observed that a significant portion of the CB, CR, and PV-positive neurons do not express detectable levels of NeuN, a widely used pan-neuronal marker (Figures 3J and 3K) (Mullen et al., 1992). In particular, a majority of CR<sup>+</sup> cells showed very weak (Figure 3K, arrowhead) or no NeuN immunoreactivity (29.1%), whereas all SMI-32<sup>+</sup> cells (Figures 3J and 3K) were NeuN-positive. These results suggest that NeuN expression may be neuronal-type-specific in adult human visual association cortex. We also found a small number of CB<sup>+</sup> cells and PV<sup>+</sup> cells co-expressing SMI-32, a widely used pyramidal neuronal marker (Table S2) (Campbell and Morrison, 1989). Five CB<sup>+</sup>/PV<sup>+</sup> cells were identified as quadruple-positive (NeuN<sup>+</sup>/SMI-32<sup>+</sup>/CB<sup>+</sup>/PV<sup>+</sup>) cells (Figure 3G). All of the CB<sup>+</sup> cells and PV<sup>+</sup> cells co-expressing SMI-32 were localized in cortical layers III and IV. These results demonstrate the power of SWITCH as a tool for 3D proteomic profiling of intact biological samples at single cell resolution.

Structural relationships between vasculature and brain cells have been a topic of interest in a broad range of basic and clinical research. Many previous studies obtained the cell-to-vessel distance from 2D images or small tissue volumes, which may hinder precise measurement of such 3D properties. Moreover, in

many studies, separate measurements from different tissues needed to be compared without considering individual variabilities in local vasculature geometry. There has been no direct comparison of 3D cell-to-vessel distance among diverse cell types within the same intact tissue.

Using the proteomic imaging capability of SWITCH, for the first time, we were able to directly measure cell-to-vessel distances for six different cell types within a single intact tissue (Figures 3L–3O). As expected (McCaslin et al., 2011), GFAP<sup>+</sup> astrocytes had a shorter mean distance than NeuN<sup>+</sup> neurons (Figure 3L). CB<sup>+</sup> and PV<sup>+</sup> cells were also more closely localized near blood vessels than NeuN<sup>+</sup> cells, but the difference was relatively small. Figure 3M shows that vascular density is not uniform along the cortex. However, the extravascular pixel-to-vessel distance ( $D_p$ ), which we defined as a reference parameter to reflect the effect of the 3D vascular geometry (Figure 3M, right), did not show an inverse relationship with vascular density. This result may suggest that 3D vessel geometry is an important parameter to be considered in understanding a given vascular environment. In fact, cell-to-vessel distance profiles of many cell types closely followed the  $D_p$  profile (GFAP<sup>+</sup>,  $D_G$ , and NeuN<sup>+</sup>,  $D_N$ , shown in Figure 3M). In particular, when  $D_p$  was subtracted from cell-to-vessel distances ( $D_x$ ) to cancel the influence of vascular geometric variation,  $D_x - D_p$  turns out to be very consistent throughout cortical depth (Figure 3N). We further examined the distance distribution profiles for all cell types (Figure 3O). All profiles showed similar characteristic curves, which can be seen when objects are randomly located in a 3D space (Manzo et al., 2014). We could not observe any cell-type-specific distribution profile or bi- or multi-modal distribution pattern in this sample. Together, these data demonstrate that SWITCH can be used for high-dimensional quantitative phenotyping of human clinical samples.

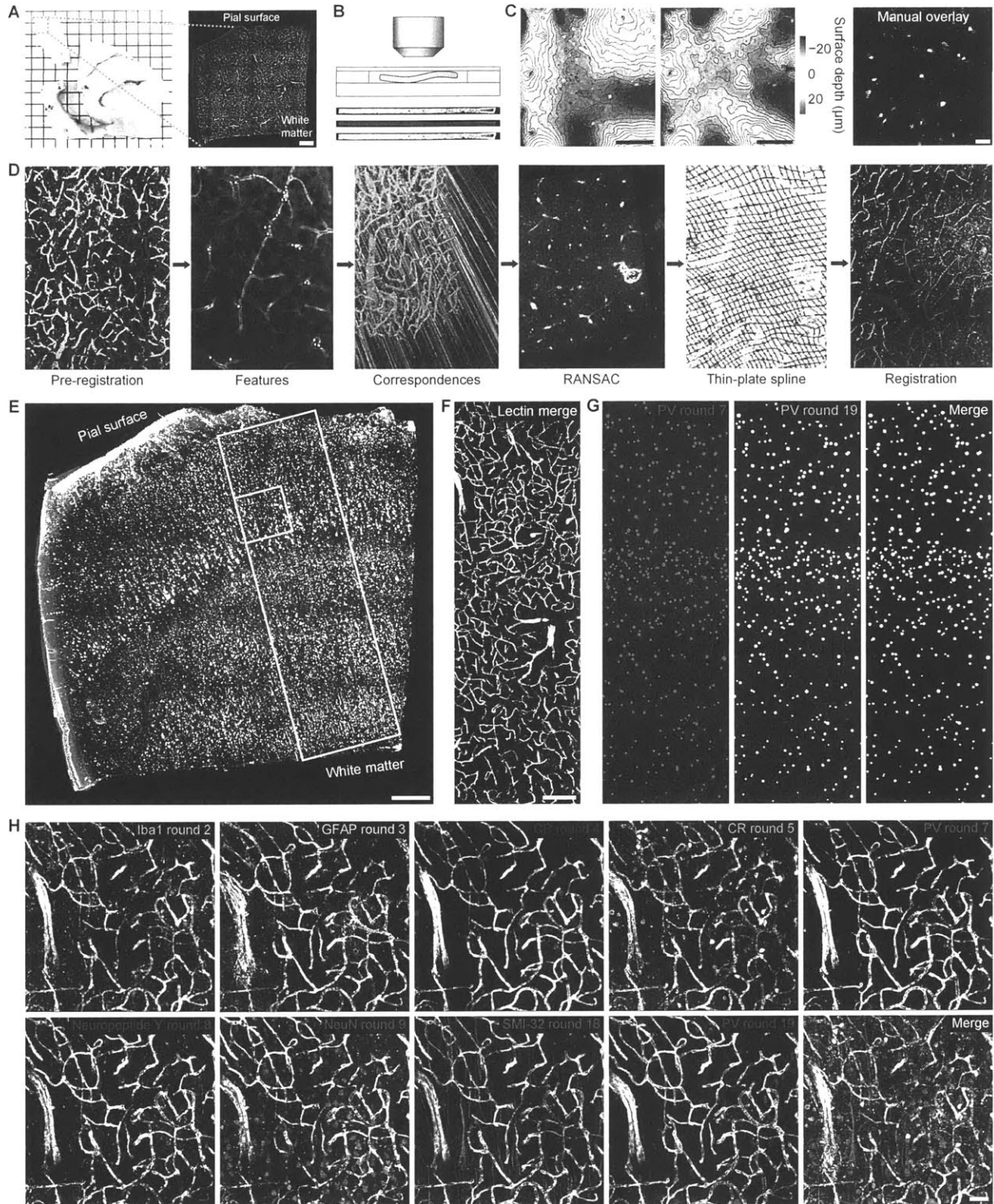
**Table 1. Multiplexed Imaging Rounds.**

Round	Excitation wavelength (nm)		
	405	488	647 <sup>a</sup>
1	DAPI	Lectin	Iba1
2	DAPI	Lectin	Iba1
3	DAPI	Lectin	GFAP
4	DAPI	Lectin	Calbindin
5	DAPI	Lectin	Calretinin
6	DAPI	Lectin	Fluoromyelin
7	DAPI	Lectin	Parvalbumin
8	DAPI	Lectin	Neuropeptide Y
9	DAPI	Lectin	NeuN
10	DAPI	Lectin	Dil D7777
11	DAPI	Lectin	SOM
12	DAPI	Lectin	Cholecystokinin
13	DAPI	Lectin	NMDAR1
14	DAPI	Lectin	NC3 $\beta$ T
15	DAPI	Lectin	GAD67
16	DAPI	Lectin	Npas4
17	DAPI	Lectin	NACHR
18	DAPI	Lectin	SMI-32P
19	DAPI	Lectin	Parvalbumin
20	DAPI	Lectin	Iba1
21	DAPI	Lectin	GFAP
22	DAPI	Lectin	SMI-312

<sup>a</sup>Iba1, ionized calcium-binding adapter molecule 1; GFAP, glial fibrillary acidic protein; SOM, somatostatin; NMDAR1, N-methyl-D-aspartate receptor 1; NC3 $\beta$ T, neuronal class III  $\beta$ -tubulin; GAD67, glutamic acid decarboxylase 67; Npas4, neuronal PAS domain protein 4; NACHR, nicotinic acetylcholine receptor.

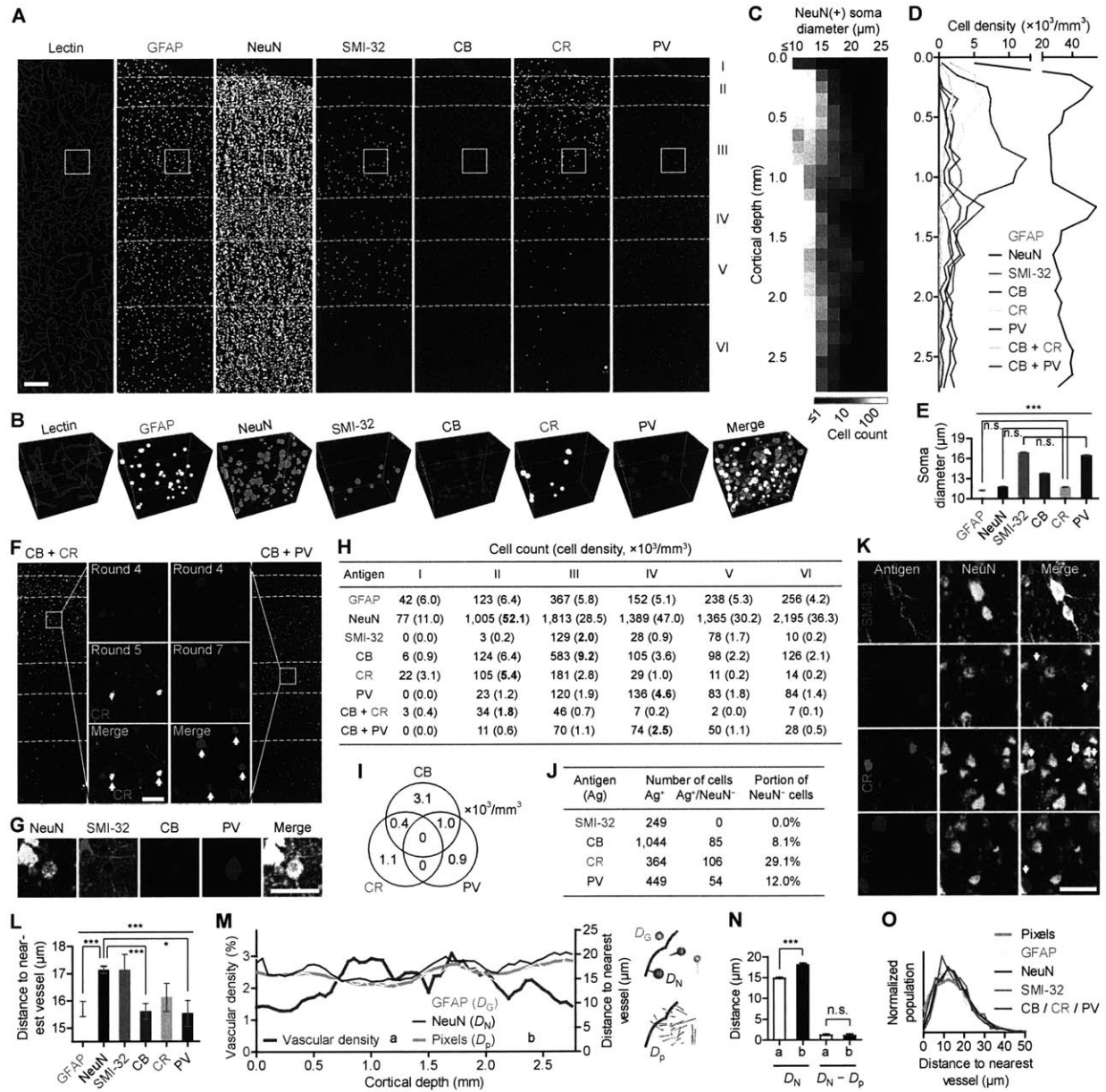
**Figure 2. SWITCH and Co-registration Algorithms Enable Highly Multiplexed Imaging at Single-cell Resolution.** (A) The left image shows formalin-fixed postmortem human brain tissue (visual association cortex, Brodmann area 18). The right image shows a 100- $\mu\text{m}$  section of this brain tissue after SWITCH processing. Scale bars, 5 mm (left), 300  $\mu\text{m}$  (right). (B) Natural warping of the sample during imaging was enabled by mounting within a chamber space larger than the size of the sample. Representative cross-sections of the sample after several rounds of imaging are shown. Sample thickness, 100  $\mu\text{m}$ . (C) Surface contour maps showing warping of the sample between imaging rounds. Attempted manual overlay of two PV datasets shows that sample warping is too severe for single-cell registration without computational correction. Scale bars, 50  $\mu\text{m}$ . (D) A flow diagram depicting the sequence of events for automated co-registration of datasets. (E) Fully co-registered image showing an overlay of 9 rounds of immunostaining. A total of 22 rounds of staining of the same tissue was achieved. R#2 (Iba1), R#3 (GFAP), R#4 (calbindin, CB), R#5 (calretinin, CR), R#7 (PV), R#8 (Neuropeptide Y), R#9 (NeuN), R#18 (SMI-32), and R#19 (PV) were used for co-registration and subsequent quantitative analysis (see Figure 3). The boxed regions indicate the ROI's shown in panels (F–H). Scale bar, 300  $\mu\text{m}$ . (F) Vasculature labeling from 9 rounds of staining after co-registration. Scale bar, 200  $\mu\text{m}$ . (G) PV cell counts between rounds 7 and 19. After 12 rounds of imaging, 99% of previously detected PV<sup>+</sup> cells were again detected and shown to overlay after co-registration of the datasets. (H) Images of individual channels with corresponding vasculature labeling. Scale bar, 50  $\mu\text{m}$ . See also Table 1.

Figure 2. SWITCH and co-registration algorithms enable highly multiplexed imaging at single-cell resolution.



**Figure 3. SWITCH Enables Proteomic Imaging and High-Dimensional Quantitative Phenotyping of Human Clinical Samples.** (A) ROI from Figure 2E showing semi-automatically detected locations and sizes of blood vessels (lectin) and diverse cell types (GFAP<sup>+</sup>, NeuN<sup>+</sup>, SMI-32<sup>+</sup>, CB<sup>+</sup>, CR<sup>+</sup>, PV<sup>+</sup>) in human visual cortex. The identified objects are overlaid on maximum intensity-projections of raw images of the corresponding channels (dark gray). Dashed lines divide cortical layers I–VI. (B) 3D rendering of the boxed region in (A) (200  $\mu\text{m}$  wide  $\times$  200  $\mu\text{m}$  high  $\times$  104  $\mu\text{m}$  deep) showing identified cells and blood vessels. (C) A heat map of the soma size distribution of NeuN<sup>+</sup> cells, showing bimodal peaks at cortical layers III and V. (D) Density profiles of various cell types. (E) Comparison of cell sizes among different types of cells. One-way ANOVA was performed ( $***P < 0.001$ ;  $N = 1,176, 7,835, 249, 1,044, 364$  and  $449$  for each column). Post hoc tests were mostly  $P < 0.001$  except for three non-significant (n.s.) cases. (F) Distribution of neurons expressing various subsets of calcium-binding proteins in the human visual cortex. Raw images in the middle columns show CB<sup>+</sup>/CR<sup>+</sup> or CB<sup>+</sup>/PV<sup>+</sup> neurons (arrows). (G) A representative NeuN<sup>+</sup>/SMI-32<sup>+</sup>/CB<sup>+</sup>/PV<sup>+</sup> cell. (H) Cell counts and densities in different cortical layers. Cortical layers with the highest density for each neuronal channel are highlighted. (I) Cell densities for combinatorial co-expression of three interneuronal markers. (J) Statistics for NeuN<sup>-</sup> neurons. (K) Representative images showing NeuN<sup>-</sup>/CB<sup>+</sup>, NeuN<sup>-</sup>/CR<sup>+</sup>, and NeuN<sup>-</sup>/PV<sup>+</sup> cells (arrows). The arrowhead indicates a CR<sup>+</sup> cell with low NeuN immunoreactivity. (L) Comparison of cell-to-nearest vessel distances along cortical depth as measured from cell centroids to vascular boundaries. Post hoc tests following one-way ANOVA ( $P < 0.001$ ;  $N = 935, 4,101, 210, 817, 265$  and  $331$  for each column) were mostly n.s. except for three cases displayed.  $*P < 0.05$ . (M) Vascular density and distance-to-nearest vessel profiles of GFAP<sup>+</sup> or NeuN<sup>+</sup> cells along cortical depth. Mean distances from NeuN<sup>+</sup> ( $D_N$ ) and GFAP<sup>+</sup> ( $D_G$ ) cells and all extravascular pixels ( $D_p$ ) are calculated and plotted. Diagrams illustrate the calculation of the three distances. (N) Cell-to-nearest vessel distances from NeuN<sup>+</sup> cells in two regions—a ( $N = 570$ ) and b ( $N = 445$ ) in (M)—before ( $D_N$ ) and after ( $D_N - D_p$ ) correction. (O) Distribution profile of extravascular pixel- or cell-to-nearest vessel distances showing similar patterns. Three interneuronal markers are plotted together. Error bars are shown with mean  $\pm$  SEM. Scale bars, 200  $\mu\text{m}$  (A), 50  $\mu\text{m}$  (F, G, and K).

**Figure 3. SWITCH enables proteomic imaging and high-dimensional quantitative phenotyping of human clinical samples.**





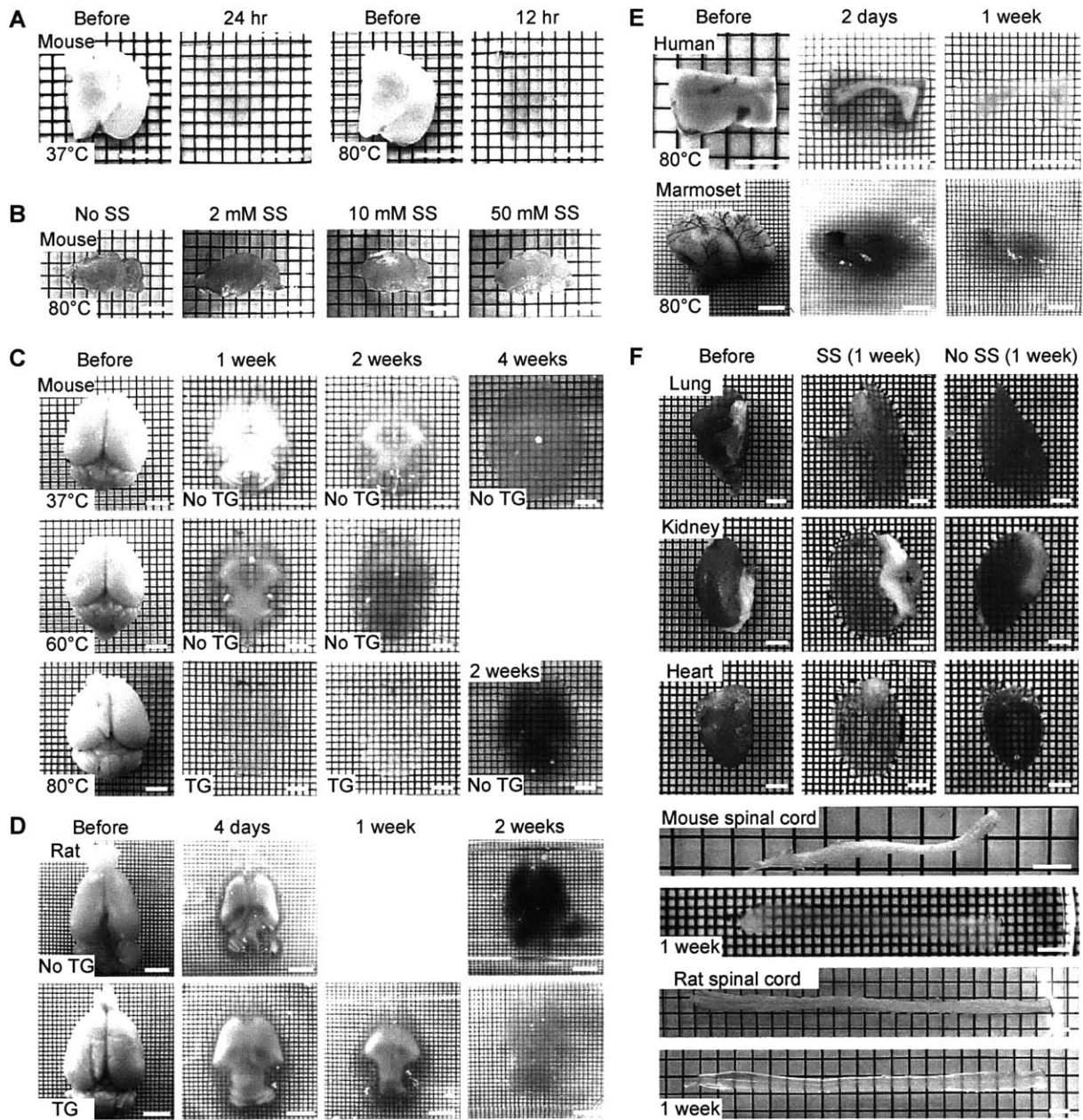
### **SWITCH Enables Simple, Rapid, and Scalable Tissue-Clearing.**

To extend the multiplexed imaging capability of the SWITCH method to large systems, we developed a simple and rapid clearing method. We hypothesized that key steps in detergent-mediated lipid removal, such as permeation of SDS through membranes, might be strongly enhanced by increasing temperature (Keller et al., 2006), and SWITCH-processed samples may endure prolonged incubation at elevated temperatures. Indeed, thermal energy drastically increased the passive clearing speed of SWITCH-processed samples without noticeable tissue damage (Figure 4A). We achieved passive clearing of a whole adult mouse brain within 4 days at 80°C (vs. 4 weeks at 37°C) (Figure 4C).

Upon prolonged exposure to high temperatures, however, samples developed a brownish hue (Friedman, 1996), which may interfere with imaging at certain wavelengths (Figures 4B–4D and 4F). We found that reducing agents, such as sodium sulfite and 1-thioglycerol, effectively mitigate tissue browning during thermal clearing (Figures 4B–4D). Using thermal clearing with the reducing agents, we successfully cleared intact adult rat brains (2 weeks) as well as human (1 week) and marmoset samples (1 week), demonstrating the versatility and scalability of the method (Figures 4D and 4E). Clearing of various rodent organs was also demonstrated with lung, kidney, heart, liver, and spinal cord (Figure 4F). The efficacy of sodium sulfite as an anti-browning agent was seen across all tissues.

**Figure 4. SWITCH Enables Simple, Rapid, and Scalable Tissue Clearing.** (A) Images of 1-mm coronal blocks of an adult mouse brain hemisphere before and after clearing at 37°C for 24 hr or 80°C for 12 hr. The lipid-extracted tissues were refractive index (RI)-matched (see SI for details). Scale bars, 3 mm. (B) Images of mouse brain hemispheres lipid-extracted at 80°C for 10 days with 200 mM SDS containing 0–50 mM sodium sulfite (SS) as an anti-browning agent. Note that the tissues were not RI-matched. Scale bars, 6 mm. (C) Images of intact adult mouse brains cleared at 37°C (top) and 60°C (middle) and 80°C (bottom) with and without 1-thioglycerol (TG). Browning in high-temperature clearing was effectively prevented by TG. Scale bars, 3 mm. (D) High-temperature (80°C) clearing of whole rat brain with and without TG. Scale bars, 6 mm. (E) Clearing of human and marmoset samples at 80°C. Scale bars, 6 mm. (F) Rapid clearing of various organs at 80°C with and without 50 mM SS. Cleared rat spinal cord is not RI-matched. Scale bars, 3 mm.

**Figure 4. SWITCH enables simple, rapid, and scalable tissue clearing.**





### **SWITCH Enables Visualization and Quantitative Analysis of Entire Myelinated Fiber Tracts**

We also sought to apply SWITCH to characterizing myelinated fiber pathways in the brain. Visualizing and analyzing neural fibers with high-resolution light microscopy can provide valuable insights into many studies (Thomas et al., 2014; Wedeen et al., 2012; Zuccaro and Arlotta, 2013), such as validating diffusion tensor imaging (DTI) and understanding the organizing principles of brain connectivity. Furthermore, quantitative analysis of myelinated fibers in 3D may benefit clinical studies and development of novel treatments for many demyelinating diseases (Steinman, 1999), such as multiple sclerosis and transverse myelitis. However, current methods for myelinated fiber visualization require either genetic labeling or a large amount of costly antibodies, limiting their utility to animal tissues or small clinical samples (Wedeen et al., 2012).

We discovered that a subset of lipids preserved in SWITCH-processed tissues (Hopwood, 1972; Roozmond, 1969) allows lipophilic dyes to selectively visualize lipid-rich membranes (Schlessinger et al., 1977). In particular, we found that long-chain dialkylcarbocyanines robustly stain myelinated axons (Figure 5A). However, when we attempted to label an intact tissue using conventional methods, we could not achieve dye penetration deeper than 100  $\mu\text{m}$  because dye molecules were depleted as they rapidly associated with abundant targets in the outer layer (Figure 5C).

We hypothesized that SWITCH may enable rapid and uniform labeling of intact tissues by synchronizing the labeling reaction globally. We first screened a range of chemicals for controlling the binding kinetics of the lipophilic dye and discovered that 10 mM SDS effectively inhibits staining (Figure 5B). This result indicates that buffers containing 10 mM SDS might have a potential to be used as a “SWITCH-Off” buffer. Using an approach analogous to SWITCH-mediated GA fixation, we thought it might be possible to allow

dye molecules to disperse uniformly throughout a sample in the SWITCH-Off buffer and then activate global probe-target binding with the SWITCH-On buffer (Figure 5D).

To test this approach, we first incubated a 1-mm-thick mouse brain block in PBST containing 10 mM SDS and lipophilic dyes for 24 hr at 37°C (SWITCH-Off step). Then, we moved the tissue to PBST and incubated it for 3 hr at 37°C (SWITCH-On step). The result was strikingly uniform labeling of all the myelinated axons within the sample (Figure 5D). Myelinated fibers were clearly visible throughout the depth while the control tissue showed signal only from the surface (Figure 5C).

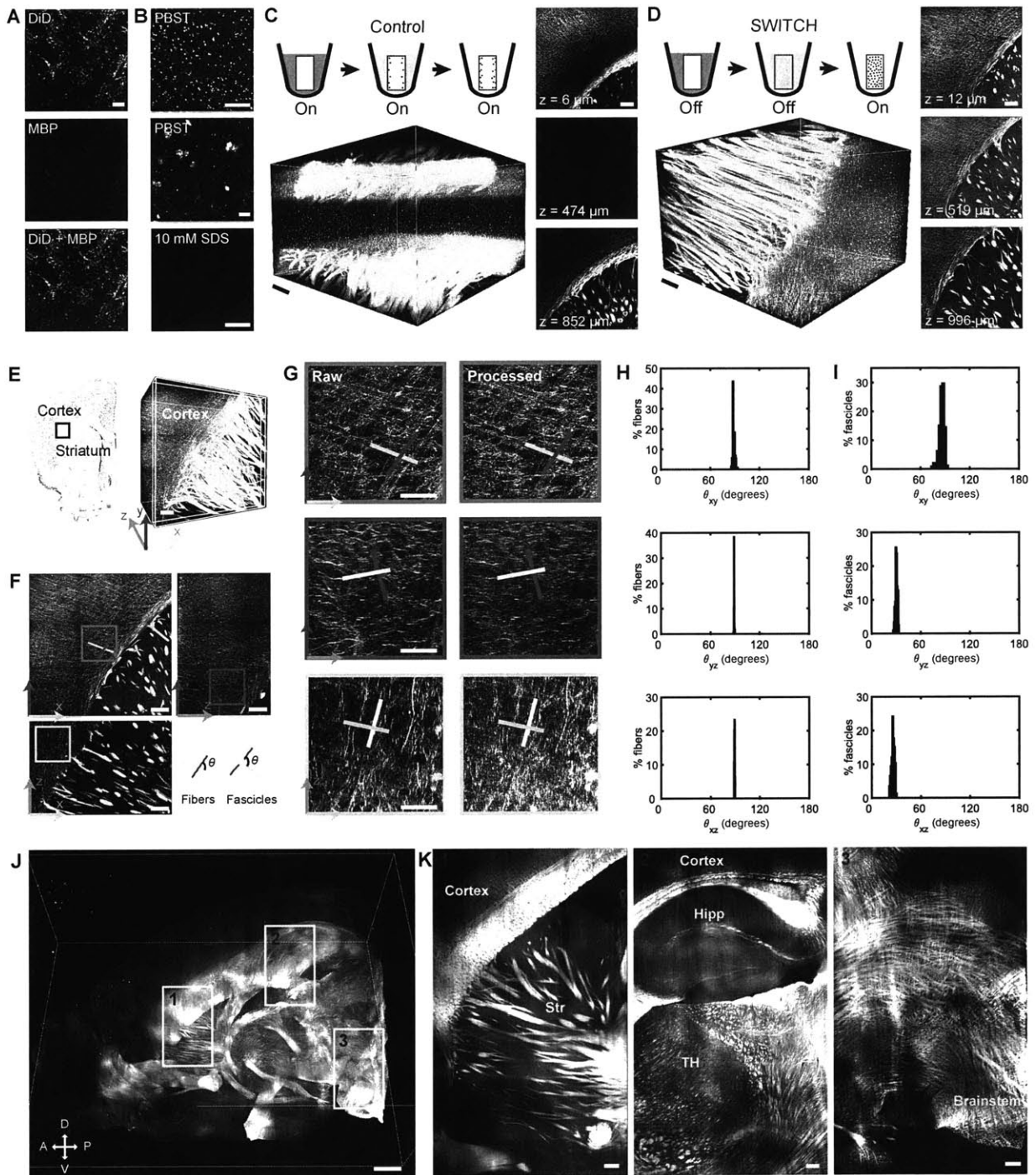
We leveraged this fiber visualization capability to investigate how fibers and fascicles are organized in a mouse brain. Previous research has shown that fibers may be organized in 3D grids (Wedeen et al., 2012). However, the structure of all of the individual fibers has not yet been studied at the microscopic resolutions and macroscopic scales necessary to visualize their 3D organization. To that end, we obtained a volume image of labeled myelinated fibers in a SWITCH-processed mouse brain coronal slice spanning from the cortex to the striatum (Figure 5E). This volume shows three main orientations of the fibers organized in a cubic grid: one radially projecting from the corpus callosum and two parallel to the corpus callosum. These three orientations are all orthogonal to one another (Figure 5F). The volume also shows fascicles that radiate from the striatum and diverge, almost at right angles, at the corpus callosum (Figure 5E). To quantify this finding in a non-biased manner, we determined the orientation of each of the fibers present in the volume and calculated the angles at which these fibers would intersect (Figure 5G). In all three dimensions, the fibers indeed oriented themselves approximately orthogonally to each other (Figure 5H). We used a similar approach to examine the fascicle orientations and found that they diverge almost orthogonally with respect to the corpus callosum in one of the axes (Figure 5I). These results are corroborated by the autocorrelation results. This finding was made possible by the high-resolution and

large-volume visualization capability of our method. A low-resolution approach would overlook the individual fibers while a low-volume approach would be unable to capture the entire connective anatomy.

We then tested whether this application of SWITCH could be scaled to larger tissues. We applied the SWITCH approach for labeling an intact mouse hemisphere, but with 4 days of incubation in PBST containing 10 mM SDS and lipophilic dyes (SWITCH-Off step) and 1 day in PBST (SWITCH-On step). We imaged this larger volume using a custom-built, high-speed light-sheet microscope (Tomer et al., 2012; Tomer et al., 2014) within 2 hours and observed uniform labeling of all myelinated fibers across the entire tissue (Figure 5J). As demonstrated, the SWITCH-labeling approach is scalable to organ-scale tissues. Just by scaling the incubation time with respect to the tissue size, we were able to label the whole tissue. The cost of the dye molecules used for labeling the hemisphere was less than one dollar. We also demonstrated that this approach can be used for visualizing myelinated fibers in spinal cords. These results show that the SWITCH-labeling method can be used to uniformly label tissues ranging from a 1-mm-thick block to an entire hemisphere for quantitative analysis.

**Figure 5. SWITCH Enables Visualization and Quantitative Analysis of Entire Myelinated Fiber Tracts.** (A) DiD and MBP staining on a SWITCH-processed mouse brain slice showing complete overlap between DiD and MBP. Scale bar, 10  $\mu\text{m}$ . (B) DiD staining with PBST or with PBS + 10 mM SDS buffer. DiD staining is completely inhibited in PBS + 10 mM SDS buffer. Green, syto16; red, DiD; scale bars, 100  $\mu\text{m}$  (top, bottom), 10  $\mu\text{m}$  (middle). (C) DiD staining of a 1-mm-thick mouse coronal block using PBST for 1.5 days at 37°C. Only tissue surface is labeled. Scale bar, 200  $\mu\text{m}$ . (D) DiD staining of a 1-mm-thick mouse coronal block using SWITCH. The sample was first incubated in DiD, 10 mM SDS containing PBS buffer for 24 hr, then moved to PBST and incubated for 0.5 day at 37°C. The whole sample is uniformly labeled. Scale bar, 200  $\mu\text{m}$ . (E) Volume image of a 1-mm-thick mouse brain coronal slice stained with DiD to visualize myelinated tracts acquired using a confocal microscope. The volume contains both the striatum and the cortex. Scale bar, 200  $\mu\text{m}$ . (F) Maximum intensity projection of the subvolume (illustrated in white in the volume image in [E]) shows fascicles from the striatum diverging at the corpus callosum and fibers near that area in the cortex forming a grid pattern. Scale bar, 200  $\mu\text{m}$ . (G) Enlarged images of the selected regions of interest in (F) shows the fibers in the cortex arranged in a grid pattern. Fibers are colorized based on orientation. Scale bar, 100  $\mu\text{m}$ . (H) Analysis of all the fibers in the entire volume shows that most fibers make an 89° intersection in xy and yz and an 88° intersection in xz. (I) Analysis of all the fascicles in the entire volume shows that they make an 87° turn in xy, a 26° turn in yz, and a 30° turn in xz. (J) Volume image of a mouse brain hemisphere stained with DiD to visualize myelinated tracts acquired using a custom-built light-sheet microscope. Scale bar, 1 mm. (K) Representative images showing individual fibers and fascicles in three different brain regions in (J). Str, striatum; Hipp, hippocampus; TH, thalamus. Scale bars, 200  $\mu\text{m}$ .

**Figure 5. SWITCH enables visualization and quantitative analysis of the entire myelinated fiber tracts.**





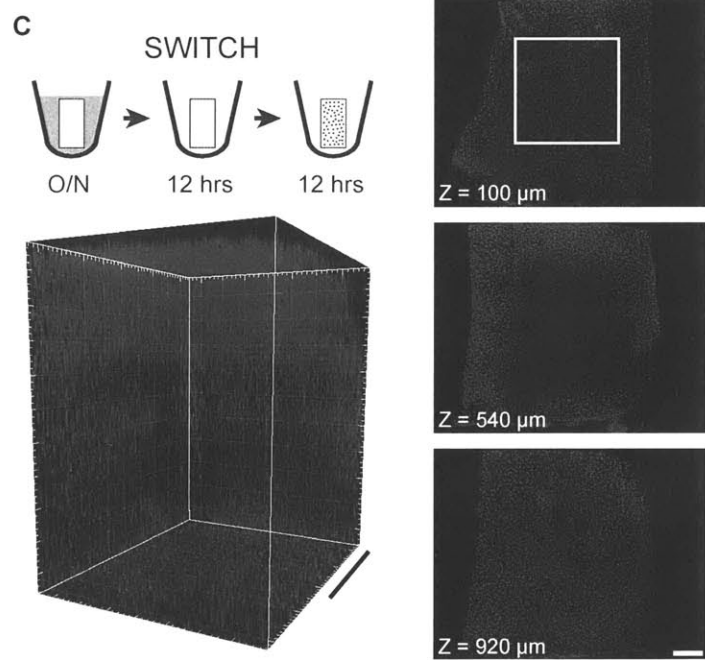
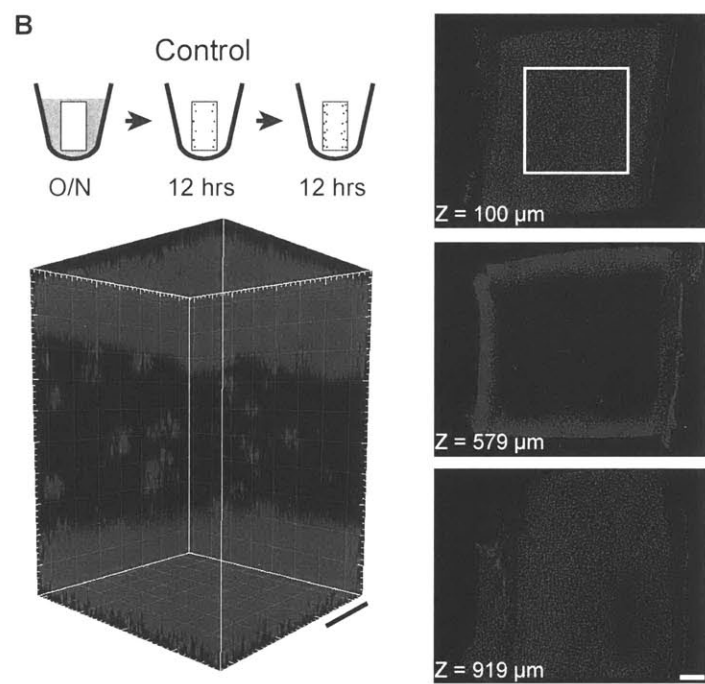
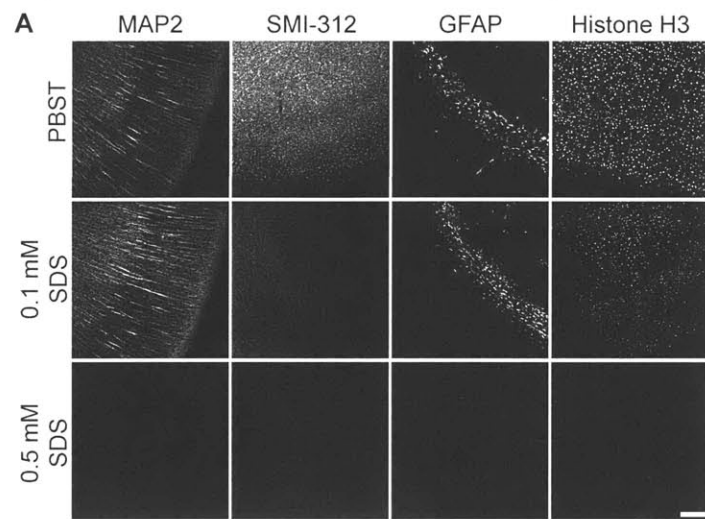
### **SWITCH Enables Scalable and Uniform Antibody Labeling**

We then asked whether SWITCH-mediated labeling could be applied to the use of antibodies. We hypothesized that SDS could again be used as an effective inhibitor of antibody-antigen binding in small concentrations. Indeed, when we assayed for antibody labeling at various concentrations of SDS, we found that 0.5 to 1.0 mM was a high enough concentration to inhibit binding for many antibodies (Figure 6A).

Based on the results of our binding assay, we chose PBS containing 0.5 mM SDS as a SWITCH-Off buffer and PBST as a SWITCH-On buffer. We hypothesized that, because very little antibody-antigen binding is occurring in the SWITCH-Off condition, antibodies would effectively be able to diffuse to equilibrium throughout the sample more rapidly than in PBST, in which antibodies are rapidly depleted at the surface (Figure 6B). To test this, we attempted to label 1-mm-thick mouse brain blocks using anti-histone H3 antibodies. We labeled one sample using a 12-hr SWITCH-Off/12-hr SWITCH-On cycle and another using a standard immunohistochemistry protocol with 12 hr of primary antibody incubation in PBST followed by a 12 hr wash. For the SWITCH-On step, antibodies were not added to PBST. The result was a large increase in penetration depth and overall signal uniformity in the SWITCH sample relative to the control (Figures 6B and 6C).

**Figure 6. SWITCH Increases Uniformity of Antibody Labeling in Thick Tissues.** (A) Antibody staining of cleared 100- $\mu\text{m}$  mouse brain sections in PBST and various concentrations of SDS in PBS. SDS effectively inhibits antibody-antigen binding in a concentration-dependent manner. Scale bar, 200  $\mu\text{m}$ . (B and C) Histone H3 staining of 1-mm-thick mouse cerebral cortex blocks in PBST (B) and using SWITCH (C). Control sample was incubated in antibody-containing PBST for 12 hr then washed for 12 hr. SWITCH sample was incubated in antibody-containing SWITCH-Off solution for 12 hr then washed in SWITCH-On solution for 12 hr. Sections from the top, middle, and bottom of the blocks are shown. 3D renderings were generated from the ROIs shown. SWITCH sample showed vast increase in uniformity of labeling compared to control. Scale bars, 150  $\mu\text{m}$  (B, left), 200  $\mu\text{m}$  (others).

**Figure 6. SWITCH Increases Uniformity of Antibody Labeling in Thick Tissues.**





## DISCUSSION

We have developed SWITCH, a simple method that enables scalable proteomic imaging of intact systems without requiring any specialized equipment or reagents. SWITCH is complementary to many pioneering technologies, each of which has its own unique advantages. For example, matrix-assisted laser desorption ionization mass spectrometry (MALDI-MS) and laser-ablation inductively coupled plasma mass spectrometry (LA-ICP-MS) allow visualization of a large subset of proteins and other biomolecules without a priori knowledge of targets. Recent advances in imaging mass spectrometry combined with immunohistochemistry (IHC) have significantly improved resolution (Angelo et al., 2014; Giesen et al., 2014), which was limited in MALDI-MS and LA-ICP-MS. This approach remarkably demonstrated analysis of more than 100 targets at subcellular resolution.

Multiplexing strategies for IHC that rely on iterative staining and elution have been developed. Among several pioneering techniques is array tomography, which involves cutting a tissue sample into tens or hundreds of nanometer-thick sections for staining and imaging (Micheva et al., 2010). These sections can be repeatedly washed and stained for probing different proteins. This powerful method yields subcellular resolution images of a small volume of tissue with fairly high multiplexing capability. Although these advanced technologies enable new approaches in studying complex biological systems, these methods require specialized equipment and are, therefore, difficult to implement in most labs.

With the aim of developing a simple and scalable method for proteomic imaging of both large animal and human samples, we first needed to devise the SWITCH method for controlling a broad range of chemical reactions in tissue processing to achieve uniform sample treatment regardless of tissue size and type. SWITCH dynamically modulates chemical reaction kinetics to synchronize the reaction time between molecules throughout the system. This strategy enables all endogenous molecular targets in a large intact

tissue to experience similar reaction conditions (time and concentration). As a result, large tissues can be uniformly processed.

The SWITCH approach takes advantage of the way certain chemicals can be reversibly and rapidly changed by simply modulating their surrounding environment. For instance, in the GA-tissue-gelling step, we were able to decrease the rate of GA-biomolecule crosslinking by two orders of magnitude by using pH 3 buffer, because primary amine groups in endogenous biomolecules are protonated at low pH and the resulting charged amine cannot react with GA (Hopwood, 1972). This pH-dependent reactivity means that after uniformly dispersing GA in a tissue at low pH, we can “switch-on” inactivated amine groups by changing the amine’s surrounding environment to a neutral-pH buffer. At neutral pH, charged amine groups are rapidly deprotonated and become reactive. In the case of human samples or animal samples that were previously PFA-fixed for a different purpose, this simple strategy enables all the endogenous biomolecules in a large intact tissue to simultaneously experience a similar GA-fixation/gelling condition. PFA-fixed tissues can withstand treatment at low pH while GA molecules are introduced. In the case of non-fixed samples, we recommend that they first be fixed with PFA before exposure to acidic conditions. If perfusion is possible, it is the recommended method of sample preservation.

Uniform GA-tissue-gel formation is a crucial first step towards our goal. Fixation of large samples via traditional immersion is unlikely to uniformly preserve them because highly reactive GA molecules are depleted within the outer layers of a sample. This presents a significant problem for iterative staining-based methods that rely on the removal of imaged probes using harsh elution conditions, because non-uniform preservation results in non-uniform loss of structure and molecules throughout the process. As demonstrated, our pH-SWITCH strategy ensures exceptionally uniform preservation of biological tissues

that cannot be perfused (e.g., banked human clinical samples), meeting the requirements of proteomic imaging and quantitative phenotyping.

It has been noted that fixation with GA results in an increase in broad spectrum autofluorescence. While this autofluorescence has been low enough to allow quantitative analysis, it could be problematic in visualizing targets with low copy number. We investigated the use of sodium borohydride as a method of reducing autofluorescence, but found that the tissue damage resulting from this incubation procedure offset any benefits obtained from the modest decrease in autofluorescence that we were able to observe.

The use of reducing agents has allowed us to eliminate the issue of tissue browning during high-temperature clearing, but we also observed that excessive use of these chemicals may cause gradual tissue weakening. This is likely due to the reduction of disulfide linkages that maintain the tertiary structure of proteins within a sample, resulting in increased protein denaturation. Protein denaturation may lead to reduced sample antigenicity, but we have not found this to be an issue when using conservative amounts of reducing agents. Additionally, due to the instability of mRNA at elevated temperatures, this method of rapid clearing is not compatible with methods that require the preservation of mRNA.

Multiplexed imaging requires software to warp each experiment into a common coordinate system despite the subtle physical differences between each staining round. Variance can come in the form of rigid body changes (rotation, translation, and scale), illumination artifacts, stain quality, and tissue degradation. We observed that a feature-based algorithm gives maximum robustness across these sources of variance at the cost of increased computational requirements—a reasonable trade given the declining costs of such resources. To simplify the process, gross rigid alignments (i.e., rotating the tissue

180 degrees) are still best handled by human eye before the data is passed to the algorithm to achieve the cellular-scale registration.

SWITCH can provide a reliable way to obtain integrated high-dimensional information from intact biological samples. Using the cross-talk-free dataset, we successfully performed non-biased combinatorial expression analysis of a single human clinical tissue to unequivocally identify diverse cell-types based on their distinct protein expression patterns. Our quantitative analysis shows that CR<sup>+</sup>/PV<sup>+</sup> cells do not exist within the examined volume of the human V2 cortex. The same finding was reported in mouse visual cortex (Gonchar et al., 2007), but such co-expression patterns among calcium-binding proteins may differ among brain regions and between individuals and species (Anelli and Heckman, 2006; DeFelipe et al., 1999), which, therefore, calls for more comprehensive large-scale investigation.

We observed many NeuN-negative interneurons. NeuN, a neuron-specific RNA-binding protein known as Rbfox3 protein (Kim et al., 2009), has been widely used as a pan-neuronal marker for statistical analysis of many types of mature neurons (Baleriola et al., 2014; Pickrell et al., 2015). Only a few types of neurons are exceptions, such as cerebellar Purkinje cells, olfactory bulb mitral cells, and retinal photoreceptor cells (Mullen et al., 1992). However, even though we applied strict criteria to prevent weak NeuN<sup>+</sup> cells from being identified as NeuN<sup>-</sup> cells, substantial portions of CB<sup>+</sup>, CR<sup>+</sup>, and PV<sup>+</sup> neurons were still NeuN<sup>-</sup> while all SMI<sup>+</sup> neurons were NeuN<sup>+</sup>. This result is supported by a recent report that some CR<sup>+</sup> are not NeuN<sup>+</sup>, and CR and NeuN immunoreactivities have a negative correlation in the avian brainstem (Bloom et al., 2014). Likewise, in our experiments on human visual association cortex, cells with strong immunoreactivity against calcium-binding protein markers were frequently negative or very weakly positive for NeuN. These findings, together with a series of exceptional reports such as those on NeuN<sup>+</sup> cultured astrocytes (Darlington et al., 2008) and GFAP<sup>+</sup> neuron-like cells (Oka et al., 2015), indicate that

classical cell-type markers, particularly NeuN, may need to be used more carefully in light of their selectivity and function.

The SWITCH method has the potential to modulate a wide range of probe-target binding reactions. Probe-target interactions are governed by a multiplicity of non-covalent bonds such as hydrogen bonds, electrostatic forces, van der Waals bonds, and hydrophobic interactions (Mian et al., 1991). These weak forces can be effectively controlled by changing the surrounding chemical environment (e.g., ionic strength, pH, chemical additive, and temperature) (Kamata et al., 1996). For instance, we discovered that the addition of SDS alone, in different concentrations, can completely inhibit lipophilic dye-target and antibody-antigen binding reactions.

The SWITCH method's unique uniform-labeling capability enables quantitative analysis of large tissues that was previously only possible for thin tissue sections. Quantitative analysis relies heavily on signal intensity and SNR. Non-uniform or heterogeneous labeling would prohibit or, even worse, bias the analysis. While post hoc image processing methods could correct for small gradients in labeling (or imaging), large gradients caused by non-uniform labeling, where the surface of the tissue is saturated while the core is mostly unlabeled, would preclude image recovery. If the labeling is heterogeneous, the resulting data would be heavily biased, and no image processing methods could salvage such data in a fair way. This is why quantitative analysis of non-uniformly labeled tissues is a great challenge. However, tissues labeled using SWITCH exhibit uniform signal intensity and SNR throughout the tissue. Such a clear dataset lends itself well to quantitative analysis.

Although SWITCH enables processing of large samples, the speed of labeling is still fundamentally limited by passive diffusion. This is not of concern for smaller samples or even single-round investigation of large

samples, but multiplexed imaging of large samples becomes impractical as a result, potentially taking months or years to collect the range of desired data. Recently developed methods of stochastic electrotransport (Kim et al., 2015) could potentially be combined with SWITCH to facilitate these experiments.

Together with its simplicity, scalability, and broad applicability, our data suggest that SWITCH provides access to high-dimensional multi-scale information that may help to understand health and disease from molecules to cells to entire systems.

## **EXPERIMENTAL METHODS**

### **Mice**

Young adult male and female C57BL/6 and Thy1-eGFP-M mice were housed in a reverse 12-hr light/dark cycle with unrestricted access to food and water. All experimental protocols were approved by the MIT Institutional Animal Care and Use Committee and Division of Comparative Medicine and were in accordance with guidelines from the National Institute of Health.

### **Perfusion**

Mice were transcardially perfused with ice-cold PBS and a solution consisting of 4% PFA and 1–4% GA in PBS. Brain tissues were harvested and incubated in the same fixative solution at 4°C for 2–3 days and 2–7 hr at 37°C with gentle shaking to allow for uniform fixation throughout the sample. This incubation time is critical for mitigating the effects of variable perfusion quality and promotes uniform structural and molecular preservation of the sample throughout the SWITCH process, as samples that are not ideally preserved will experience greater loss of biomolecules and a greater degree of sample deformation.

### **SWITCH-mediated Tissue Preservation**

PFA-fixed human samples were washed in a solution consisting of 50% PBS titrated to pH 3 using HCl, 25% 0.1 M HCl, and 25% 0.1 M potassium hydrogen phthalate (KHP). This wash solution was then replaced with fresh solution with the addition of 4–10% GA. The samples were then incubated in this pH 3 solution at 4°C for 2 days with gentle shaking. The acidic pH of this solution greatly slows down the reaction speed of aldehyde fixatives. The solution was then replaced with PBS with the addition of 1–4% GA and the sample was again allowed to incubate for 2–3 days at 4°C and 2–7 hr at 37°C with gentle shaking. The sample was then washed in PBS at room temperature (RT) for 1 day with gentle shaking. After washing, reactive GA within the sample was inactivated by incubation in a solution consisting of 4% glycine and 4%

acetamide for 1 day at 37°C with gentle shaking. Finally, the sample was washed for 1 day in PBS at RT with gentle shaking.

### **GA Gelation Time Experiment**

All reagents and containers were first cooled to 4°C and handled on ice. For pH 7 gels, 10 mL of a PBS solution containing 10% BSA was made prior to GA injection. For pH 3, 10 mL of a 0.1 M KHP buffer was titrated to pH 3 with HCl. Once the pH 3 and 7 BSA solutions were prepared, GA was added to a final concentration of 4% and a timer was started. Gelation was judged by inverting the tube and inspecting for fluid flow. The time required to form rigid gels was recorded in 3 replicates of the pH 3 and 7 condition.

### **Gel Denaturation Experiment**

For acrylamide (AA) gels, 10 mL of a 4% PFA, 5–15% bovine serum albumin (BSA), 4% AA, and 0.25% VA-044 solution was prepared in PBS. The polymerization was carried out under vacuum for 2 hr at 37°C in a 15 mL tube. For GA gels, 10 mL of a 5–15% BSA and 1% GA solution was prepared in PBS and allowed to gel at room temperature for 2 hr in a 15 mL tube. For the epoxide gels, 10 mL of a 5–15% BSA and 15% epoxide (i.e., EX-313, GE31, GE22) solution was prepared in 0.1 M carbonate buffer at pH 9 and allowed to gel at 37°C for 8 hr in a 15 mL tube. Each gel was extracted from the tubes and cut into approximately 5-mm-thick disks. The disks were then washed overnight in PBST to remove any unreacted reagents. After washing, each disk was massed and photographed. The disks were then transferred to an 80°C water bath and incubated overnight. The disks were removed, massed, and photographed again.

### **Sodium Borohydride Treatment**

Sodium borohydride (SB) buffer was made immediately before use by making a 1 mg/ml SB solution with PBS. For 100- $\mu$ m sections, the tissue was treated 3 times, 10 minutes each. For whole brain, the tissue was treated 3 times, 3 hr each. For both, incubation was done at room temperature without shaking.

### **Passive Clearing with Thermal Energy**

Aqueous clearing solution containing 200 mM SDS, 10 mM lithium hydroxide, 40 mM boric acid, and a variable amount of anti-browning agent (i.e., 0–50 mM sodium sulfite or 0–0.5% [w/v] 1-thioglycerol) was titrated to pH 9 using sodium hydroxide before use. For high temperature clearing, samples were incubated in 40 mL of clearing solution for 8 hr at RT with gentle shaking to allow for the anti-browning agent to diffuse throughout the tissue. Samples were then transferred to a water bath set at 60–80°C. The clearing buffer was replaced if any noticeable color was observed in solution at any point during clearing. To remove the remaining anti-browning agent and SDS after clearing, the samples were washed at 37°C for 24 hr in 40 mL PBST containing 0.02% sodium azide as a preservative.

### **mRNA FISH**

Mice were perfused with ice-cold PBS and then with fixative (4% PFA and 1% GA in PBS). Brains were incubated in the fixative for one day at 4°C and then 6 hr at RT for post-fixation. Coronal sections were prepared with a vibratome and sections were inactivated at RT for 6 hr, followed by tissue clearing under 37°C or 70°C. All solutions were prepared by using diethylpyrocarbonate (DEPC)-treated water. Digoxigenin- and 2,4-dinitrophenol (DNP)-labeled *fos* cRNA probes were detected using horseradish peroxidase-conjugated antibodies. FISH signals were visualized using a tyramide amplification kit (Perkin Elmer).

### **Refractive Index Matching**

A customized refractive index (RI)-matching solution was made by dissolving 50 g diatrizoic acid, 40 g n-methyl-d-glucamine, and 55 g iodixanol per 100 mL water. Cleared samples were incubated in 10 mL of this solution at RT with gentle shaking for 2 days prior to imaging, replacing the solution after the first day. The listed components and their proportions were chosen to adjust the pH and RI for ideal optical clearing (basic pH with RI near 1.47) as well as optimize the osmolarity of the solution to reverse the sample expansion observed after clearing. The contrast agents, diatrizoic acid and iodixanol, significantly affect the RI of the solution, while n-methyl-d-glucamine is used to adjust the pH to more basic values. All components were considered when optimizing for osmolarity. RI was measured using an Abbemat WR/MW automatic multiwavelength refractometer.

### **Mounting and Imaging**

To facilitate the use of long working distance immersion objectives, samples were mounted between a slide glass and a glass-bottom Willco dish. Blu-Tack adhesive was rolled into a cylindrical shape of a thickness slightly greater than that of the sample and was placed in a circular orientation on the slide glass with a small opening to allow addition of immersion medium after chamber construction. The sample was placed within the Blu-Tack circle and the Willco dish was secured onto the adhesive, pressing just firmly enough to make slight contact with the sample. This contact prevents the sample from moving during the imaging process, but minimizes sample deformation. For multiplexed staining experiments, contact was not made with the sample. Taking care to avoid introduction of bubbles, RI-matching solution was injected to fill the void space, and the opening was then closed using fast-curing epoxy glue. Three microscope systems were used for the experiments in this study:

- i. Olympus two-photon microscope system (FV1200MPE) equipped with a 25× CLARITY-optimized objective (prototype; NA, 1.0; WD, 8.0 mm), a 10× CLARITY-optimized objective (XLPLN10XSVMP; NA,

- 0.6; WD, 8.0 mm), a 10× water-immersion objective (NA, 0.30; WD, 3.6 mm), and a 40× oil-immersion objective (UPLSAPO40XS; NA, 1.25; WD, 0.3 mm). 405, 488, and 635 nm 1p lasers were used;
- ii. Leica TCS SP8 microscope system equipped with a white-light laser, spectral detection system, a 20× water-immersion objective (NA, 0.50; WD, 3.5 mm) and a 25× water-immersion objective (NA, 0.95; WD, 2.4 mm).
  - iii. Custom-made light-sheet microscope equipped with 10× CLARITY-optimized objective (modified from Tomer et al., 2012).

Sample datasets were visualized with IMARIS (Bitplane).

### **Sample Delabeling**

Imaged samples were delabeled in clearing solution at 60–80°C (elution condition) for 1–2 days for large samples and overnight (O/N) for thin samples. Sulfites were added for large samples to prevent browning during the extended delabeling process.

### **Protein Loss Assay**

Mouse brain samples were prepared using various preservation methods, hemisected, and then cut into 1-mm sections. The collection of sections from each hemisphere was massed and then placed into 5 mL of 200 mM SDS clearing solution. The samples were incubated at 37°C with gentle shaking for 2 weeks. A small aliquot was taken from each tube and analyzed using the Bio-Rad DC protein assay kit to quantify the degree of protein loss from the samples.

### **Microstructure Preservation Assay**

A Thy1-eGFP-M mouse was perfused with SWITCH fixative solution and the sample was cut into 1-mm sections. The eGFP expression on the surface of a section was imaged using confocal microscopy and then sample was then subjected to clearing under harsh conditions (200 mM SDS, 80°C) for 1 day. The sample was then labeled using anti-eGFP antibodies and the same region was imaged again using confocal microscopy.

### **Macrostructure Preservation Assay**

Samples processed using SWITCH and CLARITY were cut in 1-mm sections and subjected to clearing under harsh conditions for 1 day. The samples were then mounted in a chamber larger than the size of the sample to prevent compression and imaged using confocal microscopy. RI-matching solution was used to facilitate imaging of the sample. Cross-sections from the samples were visualized using IMARIS.

### **Human Tissue Samples**

Samples of fixed autopsy tissue were obtained from the Neuropathology Core of the Massachusetts Alzheimer Disease Research Center. Tissue was collected and banked in accordance with approval from the local Institutional Review Board. All samples studied came from subjects without evidence of neurologic disease on clinical grounds at the time of death and without evidence of significant disease processes upon full neuropathologic examination.

### **Multiplexed Labeling of Thin Samples**

A human clinical sample containing visual cortex was obtained and processed using SWITCH. After fixation, 100- $\mu$ m sections were obtained from the sample and cleared under harsh conditions. In each round, the sample was labeled with DAPI, DyLight 488-conjugated lectin, and a variable antibody using standard

immunolabeling procedures. The sample was mounted in a chamber larger than the size of the sample, imaged using confocal microscopy, and then delabeled under harsh conditions O/N. RI-matching solution was used to facilitate imaging of the sample.

### **Co-Registration of Multiplexed SWITCH Experiments**

To register the set of SWITCH experiments from a single tissue, one of the experimental rounds for a tissue is arbitrarily chosen as the fixed reference to which the rest of the experiments will be registered. Each experiment has one fluorescence channel dedicated to lectin, which allows the software to identify distinctive points in the vasculature in order to achieve the fine morphological adjustments across the tissue volume. We used a 3D Harris Corner detector (Harris and Stephens, 1988) to find those keypoints and a 3D modification of the SIFT descriptor (Lowe, 2004; Scovanner et al., 2007) to calculate correspondences. For robustness, we instituted a variation of RANSAC (Fischler and Bolles, 1981) to test affine transformations on local subvolumes, confirming that keypoint correspondences between experiments were legitimate. Finally, with the validated keypoints, a thin plate spline interpolation (Bookstein, 1989) was implemented to warp the tissue in a physically plausible manner.

Each experiment was processed individually by eye before using software to calculate the registration: The size of the interrogated tissues, approximately  $1 \text{ mm}^3$  in volume with  $1.09 \mu\text{m} \times 1.09 \mu\text{m} \times 1.99 \mu\text{m}$  resolution, required imaging subvolumes that were stitched together using the Leica or Olympus microscope software. The resulting tissue volume, a 4-dimensional object for the three spatial coordinates and the fluorescence channel, was examined by human eye using FIJI (Schindelin et al., 2012) to ensure image quality and a common orientation across experiments. Additionally, a rectangular crop was made around the tissue to remove unnecessary, blank voxels. Each individual experiment was then processed using a MATLAB computational pipeline developed for SWITCH and shared online via Github (<https://github.com/dgoodwin208/Registration>).

The registration pipeline has five primary steps based on the Lectin channel of each experiment. First, the image volume is partitioned into 25 subvolumes for parallelization of work and robustness checking in later steps. Each subvolume then identifies distinguishable keypoints using a 3D Harris Corner Detector and uses a 3D modification of SIFT written by Scovanner (<http://www.cs.ucf.edu/~pscovann/>) to create a descriptor vector associated with the keypoint. Note that we calculated keypoints and descriptors at multiple scale levels, achieved by convolution with Gaussian kernels of progressive size, to ensure a sufficient degree of scale invariance to the detected descriptors to successfully find matches despite differences in microscope setups across experiments. The calculations for keypoints and descriptors was often calculated in parallel across subvolumes to save time.

The third step is that each subvolume searches for corresponding keypoints in the appropriate subvolume in the reference experiment using the SIFT metric for measuring similarity between descriptors. To accomplish this we used the open-source VLFeat (<http://www.vlfeat.org>) implementation of SIFT matching algorithm. The fourth step is that the keypoint correspondences are validated via calculating affine transformations of random subsets of 4 corresponding keypoints, and the number of inliers of the resulting transformation assessed by a voxel distance threshold of 3 pixels. Each time a pair of corresponding points is counted as an inlier, it receives a vote, and after the order of  $10^6$  affine transformations, correspondence pairs with at least 80% of the votes of the highest voted pair are kept as legitimate correspondences. Finally, the validated correspondences are used to calculate a thin plate spline for the entire volume using an open-source TPS implementation written by Yang, Foong and Ong ([http://www.mathworks.com/matlabcentral/fileexchange/47409-glmdtps-registration-method/content/GLMD\\_Demo/src/TPS3D.m](http://www.mathworks.com/matlabcentral/fileexchange/47409-glmdtps-registration-method/content/GLMD_Demo/src/TPS3D.m)), resulting in a highly accurate warp to match the morphology of the reference experiment.

### **Semi-automatic Identification of Cells and Blood Vessels**

Image volumes were displayed and analyzed using custom-built graphical user interface software developed with Delphi XE4 (Embarcadero Technologies). Each image section was preprocessed to correct the inhomogeneous illumination at each image tile. In detail, we subtracted the mean intensity of a  $100 \times 100 \mu\text{m}^2$  window centered to each pixel from its intensity to uniformize the background intensity. A different algorithm was devised specifically for each marker to semi-automatically detect the centroid location and soma size of all cellular objects and vascular pixels. In general, a spherical soma volume was isolated according to the best contrast between intrasomal pixels and background pixels by increasing the size of concentric spheres, and the soma size was determined as the spherical diameter. After this automatic detection process, we corrected misidentified cell bodies manually, and the portion of the correction was less than 10%. We applied normalization of foreground signal and a Gaussian filter to the NeuN channel prior to the analysis. SMI-32<sup>+</sup> cells were fully recognized manually according to their characteristic feature of the soma connected to a vertically oriented fiber with a large nuclear shadow, and the determination of their coordinates and soma sizes was aided by an automation module of the software. Each section in the lectin channel was converted to a vascular pixel mask image according to a customized threshold, and unconnected small clusters of pixels were removed.

### **Quantitative Analysis of the Co-registered Image Channels**

We used a series of custom-built software developed with Delphi XE4 for the quantitative analysis. For co-expression analysis of two or more markers, an initial decision was made by checking whether the centroids of cells in each channel fell within a 5- $\mu\text{m}$  distance. This classification was then manually verified with a quick review software tool. Especially, NeuN<sup>-</sup> neurons were carefully reviewed, and any weak NeuN signal that changed synchronously with the other marker signal was identified as NeuN<sup>+</sup>. Cell density, vascular density, and cell- or pixel-to-vessel distance along cortical depth were obtained from their

average of 50- or 100- $\mu\text{m}$  window with a 50- or 100- $\mu\text{m}$  interval, and data points of less than 10 objects were excluded from plotting. Cell and vascular densities were corrected to exclude the dead volume outside the tissue in the ROI. The cell-to-vessel distance was calculated as a distance from the centroid location of the cell to the nearest vascular pixel. Cells or pixels positioned at the sections containing any incomplete vascular information ( $z \leq 24 \mu\text{m}$  or  $z \geq 80 \mu\text{m}$ ) were excluded from the analysis of distance to nearest vessel. The distribution profile of cell-to-vessel distance was obtained with a 3- $\mu\text{m}$  interval.

### **SWITCH-mediated Myelinated Fiber Labeling**

To create a DiD solution for myelinated fiber labeling, 1 mg of DiD powder was dissolved in 200  $\mu\text{L}$  of a solution consisting of 10 mM SDS in PBS (SWITCH-Off). For 1-mm mouse sections, samples were incubated in SWITCH-Off solution O/N with gentle shaking at 37°C. The solution was replaced with a volume of fresh SWITCH-Off buffer that was sufficient to cover the sample, and 1  $\mu\text{L}$  of the DiD solution was added. The sample was allowed to incubate for 1 day at 37°C with gentle shaking, at which point the sample was moved to a large volume of PBST (SWITCH-On) for 1 day at 37°C with gentle shaking. The sample was imaged using confocal microscopy. RI-matching solution was used to facilitate imaging of the sample.

For mouse hemispheres, the sample was incubated in SWITCH-Off solution at 37°C O/N with gentle shaking and then transferred to a volume of fresh SWITCH-Off solution sufficient to cover the sample, at which point 2  $\mu\text{L}$  of the DiD solution was added. The sample was incubated in this solution at 37°C for 4 days with gentle shaking and then moved to a large volume of SWITCH-On solution for 1 day at 37°C with gentle shaking. RI-matching solution was used to facilitate imaging of the sample.

### Orientation Analysis of Myelinated Fibers

Analysis was performed on planar images in the  $xy$ ,  $yz$ , and  $xz$  planes using OrientationJ (<http://bigwww.epfl.ch/demo/orientation/>). Specifically, OrientationJ was used to calculate the preferred orientation of each pixel (ranging from  $-90^\circ$  to  $90^\circ$ ) using the corresponding finite difference gradient. This generates planar images whose pixel values correspond to the angular component in that plane (i.e.,  $xy$  planar image contains  $\vartheta_{xy}$ ). After obtaining this orientational information in  $xy$ ,  $yz$ , and  $xz$  for all slices, the separate components of the orientation (i.e.,  $\vartheta_{xy}$  contains  $x$  and  $y$  components of the orientation) are added together to yield three-dimensional orientation vectors. The orientation vectors represent the orientations of the fibers and the fascicles. These orientation vectors can be binned according to their angles to yield information about how the fibers and the fascicles are distributed in terms of their orientation. This information can then be used to predict what angle of intersection these fibers make. Specifically, each peak in the histogram is identified and the subpopulation is estimated based on the FWHM. These are then assigned to either fibers or fascicles based on observation (i.e., in the  $xy$  plane, the image shows that fibers make a vertical/horizontal grid while the fascicles make more of a diagonal/divergent pattern; this means that the peaks near  $0$  and  $90$  (which is equivalent to  $-90$ ) correspond to the fibers, and the peaks near  $-45$  and  $45$  correspond to the fascicles). After obtaining the total populations of the entire volume, the intersections are estimated by subtracting the corresponding two peaks and then scaling that result by the FWHM. Then, assuming that all fibers and fascicles have similar pixel counts, the fraction of fibers making certain intersections can be determined.

### **Autocorrelation Analysis of Myelinated Fibers**

The analysis using the finite difference gradient is a nonlinear process that may introduce error to the analysis. The error is compounded by the fact that the z-resolution of the volume is almost three times lower than the x- and y-resolutions. A more accurate approach would be to use autocorrelation. (The finite difference gradient acts as a high pass filter for the autocorrelation.) Autocorrelation would show all the peak distributions in a more non-biased manner. As such, we calculated the autocorrelation in the volume image using MATLAB. Specifically, we used the Fourier convolution theorem with 3DFFT and a periodic boundary condition to calculate the autocorrelation of the volume image filtered with a Gaussian window; then, we transformed the resulting autocorrelation data in Cartesian coordinates to spherical coordinates and integrated out the radial component to visualize the data.

### **SWITCH-mediated Antibody Labeling**

Samples were first equilibrated in a large volume of SWITCH-Off solution (0.5 mM SDS in PBS). Samples were then moved to a volume a SWITCH-Off solution just large enough to cover the sample and containing 20  $\mu$ L of antibody solution (for histone H3 staining of 1-mm-thick tissue blocks.) Care should be taken to ensure that the final concentration of SDS in the SWITCH-Off solution is appropriate after the addition of antibody solution. The amount of antibody solution necessary will depend on the target identity. The samples were incubated in this antibody solution for 12 hr at 37°C with gentle shaking. Samples were then transferred to 10 mL of SWITCH-On solution (PBST) and were washed for 12 hr at 37°C with gentle shaking.

## REFERENCES

- Alivisatos, A.P., Chun, M., Church, G.M., Deisseroth, K., Donoghue, J.P., Greenspan, R.J., McEuen, P.L., Roukes, M.L., Sejnowski, T.J., Weiss, P.S., et al. (2013). The brain activity map. *Science* *339*, 1284–1285.
- Anelli, R., and Heckman, C.J. (2006). The calcium binding proteins calbindin, parvalbumin, and calretinin have specific patterns of expression in the gray matter of cat spinal cord. *J. Neurocytol.* *34*, 369–385.
- Angelo, M., Bendall, S.C., Finck, R., Hale, M.B., Hitzman, C., Borowsky, A.D., Levenson, R.M., Lowe, J.B., Liu, S.D., Zhao, S., et al. (2014). Multiplexed ion beam imaging of human breast tumors. *Nat. Med.* *20*, 436–442.
- Baleriola, J., Walker, C.A., Jean, Y.Y., Cray, J.F., Troy, C.M., Nagy, P.L., and Hengst, U. (2014). Axonally Synthesized ATF4 Transmits a Neurodegenerative Signal across Brain Regions. *Cell* *158*, 1159–1172.
- Bloom, S., Williams, A., and MacLeod, K.M. (2014). Heterogeneous calretinin expression in the avian cochlear nucleus angularis. *J. Assoc. Res. Otolaryngol.* *15*, 603–620.
- Bookstein, F.L. (1989). Principal warps: thin-plate splines and the decomposition of deformations. *IEEE Trans. Pattern Anal. Mach. Intell.* *11*, 567–585.
- Campbell, M.J., and Morrison, J.H. (1989). Monoclonal antibody to neurofilament protein (SMI-32) labels a subpopulation of pyramidal neurons in the human and monkey neocortex. *J. Comp. Neurol.* *282*, 191–205.
- Chung, K., and Deisseroth, K. (2013). CLARITY for mapping the nervous system. *Nat. Methods* *10*, 508–513.
- Chung, K., Wallace, J., Kim, S.-Y., Kalyanasundaram, S., Andalman, A.S., Davidson, T.J., Mirzabekov, J.J., Zalocusky, K. a, Mattis, J., Denisin, A.K., et al. (2013). Structural and molecular interrogation of intact biological systems. *Nature* *497*, 332–337.
- Darlington, P.J., Goldman, J.S., Cui, Q.L., Antel, J.P., and Kennedy, T.E. (2008). Widespread immunoreactivity for neuronal nuclei in cultured human and rodent astrocytes. *J. Neurochem.* *104*, 1201–1209.
- DeFelipe, J., González-Albo, M.C., Del Río, M.R., and Elston, G.N. (1999). Distribution and patterns of connectivity of interneurons containing calbindin, calretinin, and parvalbumin in visual areas of the occipital and temporal lobes of the macaque monkey. *J. Comp. Neurol.* *412*, 515–526.
- Fischler, M.A., and Bolles, R.C. (1981). Random sample consensus: a paradigm for model fitting with applications to image analysis and automated cartography. *Commun. ACM* *24*, 381–395.
- Friedman, M. (1996). Food Browning and Its Prevention : An Overview. *J. Agric. Food Chem.* *44*, 631–653.

- Giesen, C., Wang, H.A.O., Schapiro, D., Zivanovic, N., Jacobs, A., Hattendorf, B., Schüffler, P.J., Grolimund, D., Buhmann, J.M., Brandt, S., et al. (2014). Highly multiplexed imaging of tumor tissues with subcellular resolution by mass cytometry. *Nat. Methods* *11*, 417–422.
- Gonchar, Y., Wang, Q., and Burkhalter, A. (2007). Multiple distinct subtypes of GABAergic neurons in mouse visual cortex identified by triple immunostaining. *Front. Neuroanat.* *1*, 3.
- Harris, C., and Stephens, M. (1988). A Combined Corner and Edge Detector. *Proc. Alvey Vis. Conf.* 1988 147–151.
- Hopwood, D. (1967). Some aspects of fixation with glutaraldehyde. A biochemical and histochemical comparison of the effects of formaldehyde and glutaraldehyde fixation on various enzymes and glycogen, with a note on penetration of glutaraldehyde into liver. *J. Anat.* *101*, 83–92.
- Hopwood, D. (1970). The reactions between formaldehyde, glutaraldehyde and osmium tetroxide, and their fixation effects on bovine serum albumin and on tissue blocks. *Histochemie* *24*, 50–64.
- Hopwood, D. (1972). Theoretical and practical aspects of glutaraldehyde fixation. *Histochem. J.* *4*, 267–303.
- Kamata, N., Enomoto, A., Ishida, S., Nakamura, K., Kurisaki, J.-I., and Kaminogawa, S. (1996). Comparison of pH and ionic strength dependence of interactions between monoclonal antibodies and bovine  $\beta$ -lactoglobulin. *Biosci. Biotech. Biochem.* *60*, 25–29.
- Kasthuri, N., Hayworth, K.J., Berger, D.R., Schalek, R.L., Conchello, J.A., Knowles-Barley, S., Lee, D., Vázquez-Reina, A., Kaynig, V., Jones, T.R., et al. (2015). Saturated Reconstruction of a Volume of Neocortex. *Cell* *162*, 648–661.
- Keller, S., Heerklotz, H., and Blume, A. (2006). Monitoring lipid membrane translocation of sodium dodecyl sulfate by isothermal titration calorimetry. *J. Am. Chem. Soc.* *128*, 1279–1286.
- Kim, K.K., Adelstein, R.S., and Kawamoto, S. (2009). Identification of neuronal nuclei (NeuN) as Fox-3, a new member of the Fox-1 gene family of splicing factors. *J. Biol. Chem.* *284*, 31052–31061.
- Kim, S.-Y., Cho, J.H., Murray, E., Bakh, N., Choi, H., Ohn, K., Ruelas, L., Hubbert, A., McCue, M., Vassallo, S.L., et al. (2015). Stochastic electrotransport selectively enhances the transports of highly electromobile molecules. *PNAS*. DOI:10.1073/pnas.1510133112.
- Leuba, G., Kraftsik, R., and Saini, K. (1998). Quantitative distribution of parvalbumin, calretinin, and calbindin D-28k immunoreactive neurons in the visual cortex of normal and Alzheimer cases. *Exp. Neurol.* *152*, 278–291.
- Lowe, D.G. (2004). Distinctive Image Features from Scale-Invariant Keypoints. *Int. J. Comp. Vis.* *60*, 91–110.

Manzo, C., van Zanten, T.S., Saha, S., Torreno-Pina, J.A., Mayor, S., and Garcia-Parajo, M.F. (2014). PSF decomposition of nanoscopy images via Bayesian analysis unravels distinct molecular organization of the cell membrane. *Sci. Rep.* *4*, 4354.

McCaslin, A.F.H., Chen, B.R., Radosevich, A.J., Cauli, B., and Hillman, E.M.C. (2011). In vivo 3D morphology of astrocyte-vasculature interactions in the somatosensory cortex: implications for neurovascular coupling. *J. Cereb. Blood Flow Metab.* *31*, 795–806.

Mian, I.S., Bradwell, A.R., and Olson, A.J. (1991). Structure, function and properties of antibody binding sites. *J. Mol. Biol.* *217*, 133–151.

Micheva, K.D., Busse, B., Weiler, N.C., O'Rourke, N., and Smith, S.J. (2010). Single-synapse analysis of a diverse synapse population: Proteomic imaging methods and markers. *Neuron* *68*, 639–653.

Mullen, R.J., Buck, C.R., and Smith, A.M. (1992). NeuN, a neuronal specific nuclear protein in vertebrates. *Development* *116*, 201–211.

Oka, Y., Ye, M., and Zuker, C.S. (2015). Thirst driving and suppressing signals encoded by distinct neural populations in the brain. *Nature* *520*, 349–352.

Pickrell, A.M., Huang, C.-H., Kennedy, S.R., Ordureau, A., Sideris, D.P., Hoekstra, J.G., Harper, J.W., and Youle, R.J. (2015). Endogenous Parkin Preserves Dopaminergic Substantia Nigral Neurons following Mitochondrial DNA Mutagenic Stress. *Neuron* *87*, 371–381.

Rah, J.-C., Bas, E., Colonell, J., Mishchenko, Y., Karsh, B., Fetter, R.D., Myers, E.W., Chklovskii, D.B., Svoboda, K., Harris, T.D., et al. (2013). Thalamocortical input onto layer 5 pyramidal neurons measured using quantitative large-scale array tomography. *Front. Neural Circuits* *7*, 177.

Renier, N., Wu, Z., Simon, D.J., Yang, J., Ariel, P., and Tessier-lavigne, M. (2014). Resource iDISCO : A Simple , Rapid Method to Immunolabel Large Tissue Samples for Volume Imaging. *Cell* *159*, 896–910.

Richardson, D.S., and Lichtman, J.W. (2015). Clarifying Tissue Clearing. *Cell* *162*, 246–257.

Roozmond, R.C. (1969). The effect of fixation with formaldehyde and glutaraldehyde on the composition of phospholipids extractable from rat hypothalamus. *J. Histochem. Cytochem.* *17*, 482–486.

Schindelin, J., Arganda-Carreras, I., Frise, E., Kaynig, V., Longair, M., Pietzsch, T., Preibisch, S., Rueden, C., Saalfeld, S., Schmid, B., et al. (2012). Fiji: an open-source platform for biological-image analysis. *Nat. Methods* *9*, 676–682.

Schlessinger, J., Axelrod, D., Koppel, D.E., Webb, W.W., and Elson, E.L. (1977). Lateral transport of a lipid probe and labeled proteins on a cell membrane. *Science* *195*, 307–309.

Scovanner, P., Ali, S., and Shah, M. (2007). A 3-dimensional sift descriptor and its application to action recognition. *15th Int. Conf. Multimed.* 357–360.

De Sousa, A.A., Sherwood, C.C., Schleicher, A., Amunts, K., MacLeod, C.E., Hof, P.R., and Zilles, K. (2010). Comparative cytoarchitectural analyses of striate and extrastriate areas in hominoids. *Cereb. Cortex* *20*, 966–981.

Steinman, L. (1999). Assessment of animal models for MS and demyelinating disease in the design of rational therapy. *Neuron* *24*, 511–514.

Sung, H., Hsu, H., Shih, C., and Lin, D. (1996). Cross-linking characteristics of biological tissues fixed with monofunctional or multifunctional epoxy compounds. *Biomaterials* *17*, 1405–1410.

Susaki, E.A., Tainaka, K., Perrin, D., Kishino, F., Tawara, T., Watanabe, T.M., Yokoyama, C., Onoe, H., Eguchi, M., Yamaguchi, S., et al. (2014). Whole-brain imaging with single-cell resolution using chemical cocktails and computational analysis. *Cell* *157*, 726–739.

Thomas, C., Ye, F.Q., Irfanoglu, M.O., Modi, P., Saleem, K.S., Leopold, D.A., and Pierpaoli, C. (2014). Anatomical accuracy of brain connections derived from diffusion MRI tractography is inherently limited. *Proc. Natl. Acad. Sci. U. S. A.* *111*, 16574–16579.

Tomer, R., Khairy, K., Amat, F., and Keller, P.J. (2012). Quantitative high-speed imaging of entire developing embryos with simultaneous multiview light-sheet microscopy. *Nat. Methods* *9*, 755–763.

Tomer, R., Ye, L., Hsueh, B., and Deisseroth, K. (2014). Advanced CLARITY for rapid and high-resolution imaging of intact tissues. *Nat. Protocols* *9*, 1682–1697.

Wedeen, V.J., Rosene, D.L., Wang, R., Dai, G., Mortazavi, F., Hagmann, P., Kaas, J.H., and Tseng, W.-Y.I. (2012). The geometric structure of the brain fiber pathways. *Science* *335*, 1628–1634.

Yuste, R. (2015). From the neuron doctrine to neural networks. *Nat. Rev. Neurosci.* *16*, 1–11.

Zuccaro, E., and Arlotta, P. (2013). The quest for myelin in the adult brain. *Nat. Cell Biol.* *15*, 572–575.

Reprinted from *Cell*, Vol. 163, Evan Murray, Jae Hun Cho, Daniel Goodwin, Taeyun Ku, Justin Swaney, Sung-Yon Kim, Heejin Choi, Young-Gyun Park, Jeong-Yoon Park, Austin Hubbert, Margaret McCue, Sara Vassallo, Naveed Bakh, Matthew P. Frosch, Van J. Wedeen, H. Sebastian Seung, Kwanghun Chung, Simply, Scalable Proteomic Imaging for High-Dimensional Profiling of Intact Systems, pages 1500-1514, Copyright (2015), with permission from Elsevier.